iScience

CellPress
OPEN ACCESS

Article

Interleukin-6 promotes microtubule stability in axons via Stat3 protein–protein interactions

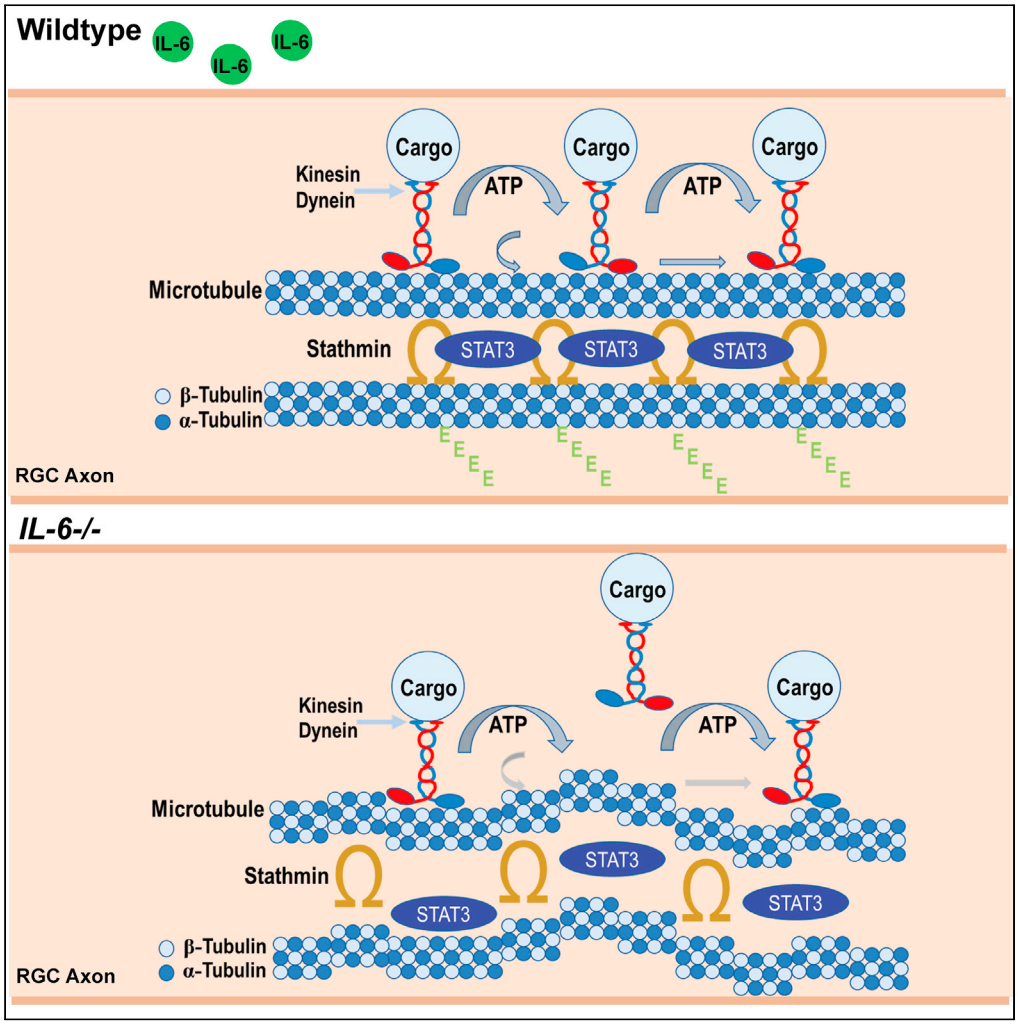

Lauren K. Wareham, Franklin D. Echevarria, Jennifer L. Sousa, ..., Peter J. Goralski, Jenna R. Gustafson, Rebecca M. Sappington

rsapping@wakehealth.edu

Highlights

IL-6 deficiency reduces the rate of axon transport by 50%

IL-6 deficiency alters microtubule morphology and post-translation modification

IL-6 deficiency dramatically reduces STAT3-stathmin interactions in axons

IL-6 promotes STAT3-stathmin interactions and stabilizes microtubules

Wareham et al., iScience 24, 103141
October 22, 2021
https://doi.org/10.1016/j.isci.2021.103141

iScience

CellPress
OPEN ACCESS

Article

Interleukin-6 promotes microtubule stability in axons via Stat3 protein–protein interactions

Lauren K. Wareham,[1,5] Franklin D. Echevarria,[2,5] Jennifer L. Sousa,[3] Danielle O. Konlian,[3] Gabrielle Dallas,[1] Cathryn R. Formichella,[1] Priya Sankaran,[1] Peter J. Goralski,[3] Jenna R. Gustafson,[3] and Rebecca M. Sappington[3,4,6,*]

SUMMARY

The interleukin-6 (IL-6) family of cytokines and its downstream effector, STAT3, are important mediators of neuronal health, repair, and disease throughout the CNS, including the visual system. Here, we elucidate a transcription-independent mechanism for the neuropoietic activities of IL-6 related to axon development, regeneration, and repair. We examined the outcome of IL-6 deficiency on structure and function of retinal ganglion cell (RGC) axons, which form the optic projection. We found that IL-6 deficiency substantially delays anterograde axon transport *in vivo*. The reduced rate of axon transport is accompanied by changes in morphology, structure, and post-translational modification of microtubules. *In vivo* and *in vitro* studies in mice and swine revealed that IL-6-dependent microtubule phenotypes arise from protein-protein interactions between STAT3 and stathmin. As in tumor cells and T cells, this STAT3-stathmin interaction stabilizes microtubules in RGCs. Thus, this IL-6-STAT3-dependent mechanism for axon architecture is likely a fundamental mechanism for microtubule stability systemically.

INTRODUCTION

IL-6 is the flagship member of the neuropoietic family of structurally related cytokines (Bauer et al., 2007). First identified as a B-cell differentiation factor (Hirano et al., 1985), it is now implicated in a number of trophic roles outside of the immune system, including neurogenesis (Leibinger et al., 2013; Borsini et al., 2015), neuronal (and glial) function (Hama et al., 1989), differentiation (Satoh et al., 1988; Sulistio et al., 2018), and proliferation (Storer et al., 2018). IL-6 is constitutively expressed in murine retina (Sims et al., 2012) and changes in IL-6 expression are associated with a variety of ocular disorders and injuries (Sanchez et al., 2003; Noma et al., 2006, 2009; Zahir-Jouzdani et al., 2017), including retinal ganglion cell (RGC) degeneration (Chidlow et al., 2012; Echevarria et al., 2017). IL-6 deficiency inhibits axon regrowth following optic nerve crush, while intravitreal application of IL-6 improves axon regrowth, suggesting that IL-6 facilitates optic nerve axon repair and regeneration in response to injury (Leibinger et al., 2013). Additionally, *in vitro* studies indicate that IL-6 can prevent RGC apoptosis and promote neurite outgrowth (Sappington et al., 2006; Chidlow et al., 2012; Leibinger et al., 2013). Despite the evidence that IL-6 can influence RGC survival, growth and repair, the role of constitutive IL-6 signaling in retina remains unexamined.

In this study, we explored the neurotropic role of IL6 in the visual system, using germline IL-6 deficiency (*IL-6−/−*). The visual system is an extension of the CNS and provides an effective tool for examining neuronal function. Our findings highlight a novel homeostatic function for IL-6 in development and maintenance of microtubule architecture in RGC axons. This function influences the overall structure of RGC axons, the rate of axon transport, and microtubule stability. Interestingly, IL-6 mediates axon structure and function via polyglutamylation state of tubulin and STAT-3 protein-protein interactions with MAPs, including stathmin and MAP-2. Our findings identify a homeostatic role for IL-6 in the structure and function of RGC axons and elucidate a mechanism for IL-6 activities in axon growth and repair. These findings have significant implications for our understanding of constitutive functions for IL-6 in the CNS with considerations for fundamental mechanisms of microtubule dynamics and therapeutic targeting of IL-6.

[1]Vanderbilt Eye Institute, Vanderbilt University Medical Center, Nashville, TN 37232, USA

[2]Neuroscience Graduate Program, Vanderbilt University, Nashville, TN 37232, USA

[3]Department of Neurobiology and Anatomy, Wake Forest School of Medicine, Atrium Health Wake Forest Baptist Medical Center, 1 Medical Center Boulevard, Winston-Salem, NC 27157, USA

[4]Department of Ophthalmology, Wake Forest School of Medicine, Winston-Salem, NC 27106, USA

[5]These authors contributed equally

[6]Lead contact

*Correspondence: rsapping@wakehealth.edu

https://doi.org/10.1016/j.isci.2021.103141

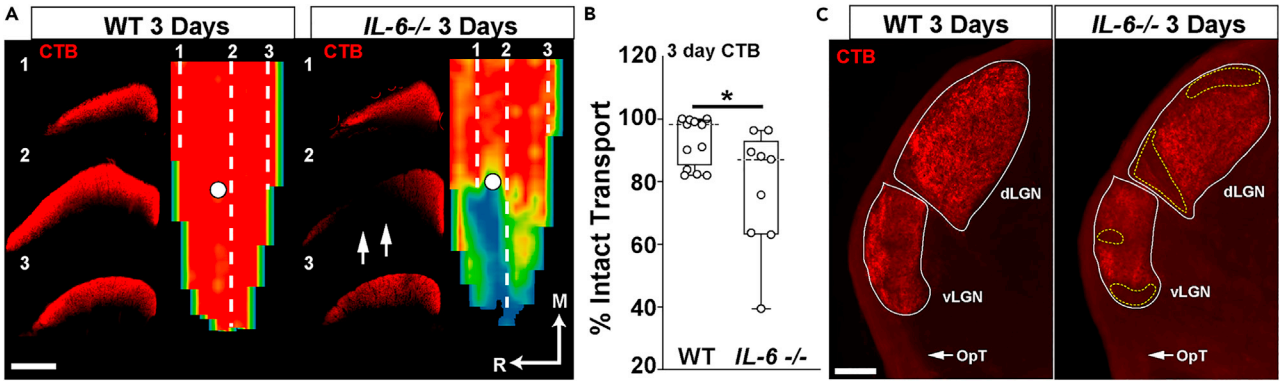

Figure 1. *IL-6−/−* mice exhibit deficits in anterograde axon transport

(A) Representative coronal sections through the superior colliculus (SC) and respective retinotopic heat maps after 3 days of CTB transport in WT (left) and *IL-6−/−* mice (right). Arrows in coronal sections indicate areas of transport deficits. Density of the CTB signal for the heat maps range from 0% (blue) to 50% (green) to 70% (yellow) to 100% (red). Numbered dashed lines in retinotopic maps indicate the location of respective coronal section and white circles indicate position of the optic disk (OD). Medial (M) and rostral (R) orientations are indicated. Scale = 500 μm for all images.

(B) Quantification of intact transport (≤70% Density). Dashed lines indicate median value and asterisks indicate $p<0.05$. n = 9–12 SC/genotype. Error bars = 95% confidence interval.

(C) Representative coronal sections through the lateral geniculate nucleus (LGN) after 3 days of CTB transport in WT (left) and *IL-6−/−* mice (right). Solid lines indicate borders of the ventral (vLGN) and dorsal (dLGN) regions of the LGN. Dashed lines indicate areas of transport deficit. Arrows indicate location of the optic tract (OpT). Scale = 500 μm.

RESULTS

IL-6 ablation produces deficits in anterograde axon transport

In mice, 70–80% of RGC axons in the optic nerve project to the superior colliculus (SC) (Dreher et al., 1985) and the neural tracer cholera toxin beta (CTB) is routinely used to trace the RGC projection and measure the rate of axon transport (Crish et al., 2010; Abbott et al., 2013; Echevarria et al., 2017). In WT mice, CTB labeled the entire SC 3 days after intravitreal CTB injection (median = 98.1%; Figures 1A and 1B). In contrast, *IL-6−/−* mice exhibited varying deficiencies in anterograde transport of CTB to the SC compared with WT mice (Figures 1A and 1B). Overall, transport to the SC was diminished by 13% in *IL-6−/−* mice (median = 87.000%), as compared to WT mice ($p = 0.014$; Figures 1A and 1B). This deficiency in transport was detectable throughout the optic projection, including the dorsal and lateral geniculate nucleus of the thalamus (Figure 1C).

IL-6 deficiency reduces the rate of anterograde axon transport

Deficits in anterograde transport often result from structural abnormalities in RGC density or termination. Thus, we examined RGC density in the retina and the spatial representation of estrogen-related receptor beta (ERRβ)+ RGC terminals in the SC. The distribution of neuron-specific beta-tubulin (βtubIII) and neurofilament (SMI-31) in RGC soma was comparable in WT and *IL-6−/−* retina (Figure 2A). Quantification of RGC soma density revealed no significant difference between genotypes (WT = 7969 ±1311 RGCs/mm^2 vs *IL-6−/−* = 7539 ±1053 RGCs/mm^2; $p = 0.284$, Figure 2A). Similarly, ERRβ immunolabeling in the SC *IL-6−/−* mice exhibited full innervation of the SC that was comparable to WT mice, even in areas with deficient CTB tracing ($p<0.05$; Figure 2B).

Next, we determined whether transport impairment was specific to CTB. In WT and *IL6−/−* mice, we examined the pattern and degree of CTB uptake in Brn3a+ RGC soma in the retina (Figure 2C). Colocalization of CTB with the RGC-specific marker Brn3a was comparable *IL-6−/−* in both WT and *IL6−/−* mice, as illustrated by Mander's colocalization frequencies of 0.9465 and 0.9746 for WT and *IL6−/−* mice, respectively (Figure 2C, inserts). CTB uptake is caveolin-dependent (Singh et al., 2003). Thus, we examined caveolin expression and localization in WT and *IL-6−/−* retina. Immunohistochemical assessment of caveolin-1 revealed similar expression in Brn3a+ RGCs (Figure 2D). Quantification of caveolin-1 protein in whole retina confirmed no significant difference in expression between WT and *IL6−/−* mice ($p<0.05$; Figure 2D). Finally, we repeated tracing of the optic projection with wheat germ agglutinin (WGA), another neural tracer that is internalized by a caveolin-independent mechanism (Margolis et al., 1981; Wan et al., 1982). With a tracing

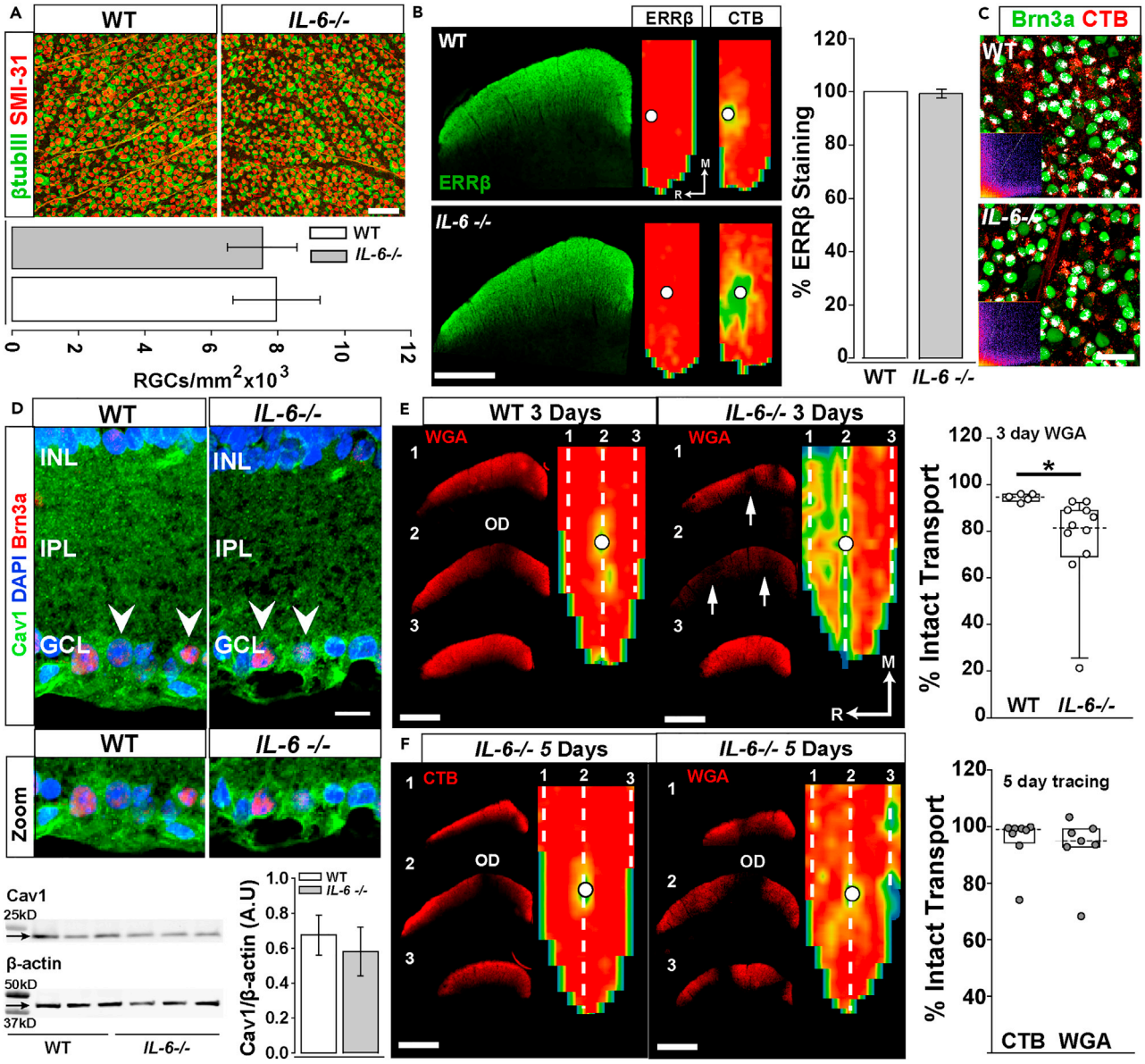

Figure 2. Axon transport deficits in *IL-6−/−* mice reflect a reduced rate of anterograde transport

(A) Representative 40X images of dual-labeled βtubIII+/SMI-31+ RGCs from mid-central/mid-peripheral retina in WT (left) and *IL-6−/−* (right) mice. Quantification of RGC density showed no significant difference between WT and *IL-6−/−* mice ($p = 0.284$, n = 5–7 images/retina, 3 retina/genotype). Scale = 50 μm. Error bars = standard deviation.

(B) Representative images of ERRβ localization in the SC (left) and quantification of ERRβ signal density (right) suggests no alteration in the structure of RGC post-synaptic inputs to the SC between WT and *IL-6−/−* mice ($p<0.05$, n = 6 SC/genotype). Scale = 500 μm. Error bars = standard deviation.

(C) Representative 100X micrographs of CTB uptake (red) in WT (top) and *IL-6−/−* (bottom) retina immunolabeled with the RGC marker Brn3a (green). Inserts: Mander's colocalization frequency. Scale = 50 μm.

(D) Top Panels: Localization of the caveolin-1 (Cav-1) to Brn3a+ RGC cell soma (red) in WT (left) and *IL-6−/−* (right) retina. Arrowheads indicate Cav-1+/Brn3a+ RGC soma. Scale = 20 μm. Bottom Panels: Immunoblotting (left) and densitometric quantification (right) of Cav-1 (22kDa) normalized to β-actin (42kDa) in retina from WT (white) and *IL-6−/−* (gray) mice. n = 3 retina/group. Error bars = standard deviation.

(E) Left Panels: Representative coronal sections through the SC and respective retinotopic heat maps after 3 days of WGA transport in WT (left) and *IL-6−/−* mice (right). Arrows in coronal sections indicate areas of transport deficits. Density of the CTB signal for the heat maps range from 0% (blue) to 50% (green) to 70% (yellow) to 100% (red). Numbered dashed lines in retinotopic maps indicate the location of respective coronal section and white circles indicate position

Figure 2. *Continued*

of the optic disk (OD). Medial (M) and rostral (R) orientations are indicated. Scale = 500 μm. Right Panel: Quantification of intact transport (≤70% Density). Dashed lines indicate median value and asterisks indicate p<0.01. n = 5–11 SC/genotype. Error bars = 95% confidence interval.
(F) Left Panels: Representative coronal sections through the SC and respective retinotopic heat maps after 5 days of CTB (left) or WGA (right) transport in *IL-6−/−* mice. OD= optic disk. Scale = 500 μm. Right Panel: Quantification of intact transport (≤70% Density). Dashed lines indicate median value. n = 5–11 SC/genotype. Error bars = 95% confidence interval.

latency of 3 days, *IL-6−/−* mice again showed significant deficiencies in WGA transport compared to WT mice (median values, WT = 94.709% intact transport, *IL-6−/−* = 81.381%, p = 0.004, Figure 2E).

Finally, we explored the possibility that there was a change in the rate of anterograde axon transport, rather than a true deficit in transport. We repeated tracing with both CTB and WGA with a tracing latency of 5 days instead of 3 days. As demonstrated in Figures 1A and 2E, full transport to the superior colliculus is achieved in WT mice after a 3-day tracing latency. After 5 days, both CTB and WGA labeling in the SC of *IL-6−/−* mice was comparable to that of WT mice (CTB = 98.945%, p = 0.671; WGA = 91.589%, p = 0.202; Figure 2F). In previously published studies, we confirmed that these *IL-6−/−* mice lack expression of IL-6 in retina (Echevarria et al., 2017). Thus, these results indicate that IL-6 deficiency slows the rate of anterograde axon transport in RGCs.

IL-6 deficiency leads to abnormal microtubule morphology in RGC axons

Since the slower rate of axon transport in *IL-6−/−* mice is not attributable to gross abnormalities in RGC soma or terminals, we examined the ultrastructure of RGC axons. Electron micrographs (67000× magnification) of optic nerve cross-sections from WT and *IL-6−/−* mice identified gross structural differences in RGC axons between *IL-6−/−* and WT mice (n = 10; Figure 3A). Microtubules in WT mice appear tightly packed, with a typical beads-on-a-string morphology (Figure 3A, white arrows), whereas *IL-6−/−* mice displayed increased spacing between microtubule bundles, and a more disorganized structure (Figure 3A, arrowheads). RGC axons in *IL-6−/−* optic nerve displayed a larger overall diameter (Dt) compared to WT optic nerve (p<0.001, Figure 3B). This increase in size was due to an approximate 12% increase in both inner axon diameter (Di; p<0.001, Figure 3B) and myelin thickness (p<0.001, Figure 3B). Thus, myelin sheath thickness increased to accommodate the larger size of axons in *IL-6−/−* mice (Figure 3B). This was confirmed by identical g-ratios (Di/Dt) between the two genotypes (WT = 0.621; *IL-6−/−* = 0.627, p = 0.356; Figure 3B).

To visualize microtubules specifically, we performed immunohistochemical staining of microtubules in the unmyelinated portion of RGC axons in whole retina with antibodies against both alpha (α)- and beta (β)-tubulin. In WT mice, immunolabeling against α-tubulin exhibited a compact, linear pattern parallel with the trajectory of the axon in both peripheral (top panel) and central regions (middle/bottom panels) of the retina (Figure 4A). However, in *IL-6−/−* mice, α-tubulin labeling unveiled aggregations of tubulin along the microtubule (Figure 4A). This observation was corroborated by a similar aggregation pattern of neuron-specific β-tubulin (Figure 4B). IL-6-related disorganization of the axon cytoskeleton appeared specific to microtubules as labeling against actin (Phalloidin; Figure S1A) and phosphorylated heavy neurofilament (pNF-H; Figure S1B) revealed a comparable linear architecture in RGC axons from both WT and *IL-6−/−* mice. Quantification of α- and β-tubulin protein levels by Western blot analysis revealed no significant difference between *IL-6−/−* mice and WT mice in both the retina and optic nerve (α-tubulin retina p = 0.191, optic nerve p = 0.05; β-tubulin retina p = 0.867, optic nerve p = 0.374; Figure 4C), suggesting that tubulin aggregation was not due to protein over-expression and deposition. Together, these data demonstrate that IL-6 deficiency leads to the disorganization of microtubule ultrastructure in axons of the optic nerve that is not dependent upon expression levels of α- or β-tubulin.

IL-6 deficiency alters the tertiary structure of microtubules via MAP localization and post-translational modifications

The proper functioning and morphology of microtubules is facilitated by the presence of MAPs (Dehmelt and Halpain, 2005; Kapitein and Hoogenraad, 2015). MAP2 is a major component of cross-bridges between neuronal microtubules and is able to stabilize microtubules and facilitate the recruitment of motor proteins for axon transport (Shiomura and Hirokawa, 1987; Hirokawa et al., 1988; Takemura et al., 1992; Felgner et al., 1997; Al-Bassam et al., 2002; Kapitein and Hoogenraad, 2015). Accordingly, we explored the possibility that tubulin aggregation in *IL-6−/−* mice was secondary to abnormalities in MAP localization. In WT

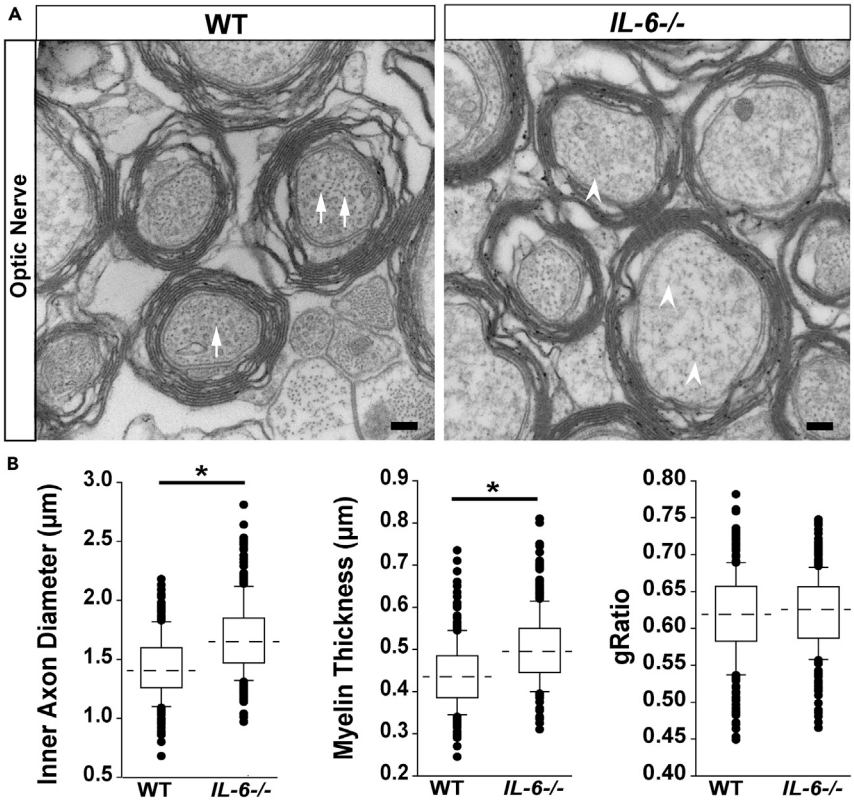

Figure 3. *IL-6−/−* mice exhibit distorted microtubule morphology in RGC axons

(A) Representative electron micrographs of RGC axons in optic nerve from WT (left) and *IL-6−/−* mice. Arrows indicate typical microtubule morphology. Arrowheads indicate abnormal microtubule morphology. 67000× magnification. Scale = 100 nm.

(B) Quantification of inner axon diameter (left) and myelin sheath thickness (middle) and g-ratio (right) of axons in WT (n = 8 nerves) and *IL-6−/−* (n = 9 nerves) optic nerve. Dashed line in boxplots indicates median value. Asterisks = $p<0.01$. Error bars = 95% confidence interval.

mice, MAP2 protein is evenly distributed throughout RGC axons in the myelinated optic nerve (Figure 5A). In contrast, immunolabeling for MAP2 is dramatically diminished in *IL6−/−* nerves (Figure 5A). Quantification of MAP2 protein expression confirmed decreased MAP2 expression in *IL6−/−* optic nerve compared with WT ($p = 0.004$, Figure 5A). Interestingly, expression of MAP2 in retina was 48% greater in *IL-6−/−* mice compared to WT ($p = 0.014$; Figure 5A). These data suggest that transcription and translation of MAP2 is likely similar in *IL-6−/−* and WT mice. However, MAP2 protein is sequestered in the retina and does not localize properly to tubulin in RGC axons of *IL-6−/−* mice.

MAP binding affinity and localization is mediated, in part, by post-translational modifications on tubulin. Polyglutamylation of tubulin is a post-translational modification that directly influences MAP2 binding to tubulin (Boucher et al., 1994; Bonnet et al., 2001). To assess levels of polyglutamylation in the optic nerve of *IL-6−/−* mice, we performed immunohistochemical staining using GT335, an antibody specific for polyglutamylated tubulin (Figure 5B). Optic nerve sections in *IL-6−/−* mice exhibited almost a complete lack of GT335 immunolabeling compared to WT mice (Figure 5B). Quantification of polyglutamylated tubulin by Western blot analysis revealed a 95% reduction in polyglutamylation levels in *IL-6−/−* optic nerve ($p<0.0001$) and a 45% reduction in the retina compared with WT mice ($p = 0.0005$; Figure 5B). These results indicate that the absence of IL-6 signaling reduces polyglutamylation of tubulin *in vivo*.

IL-6 deficiency impedes STAT3:Stathmin protein-protein interaction

To determine whether changes in MAP2 localization and β-tubulin glutamylation state manifest in MAP2-tubulin associations, we performed proximity ligation assay (PLA) in optic nerve sections against MAP2 and

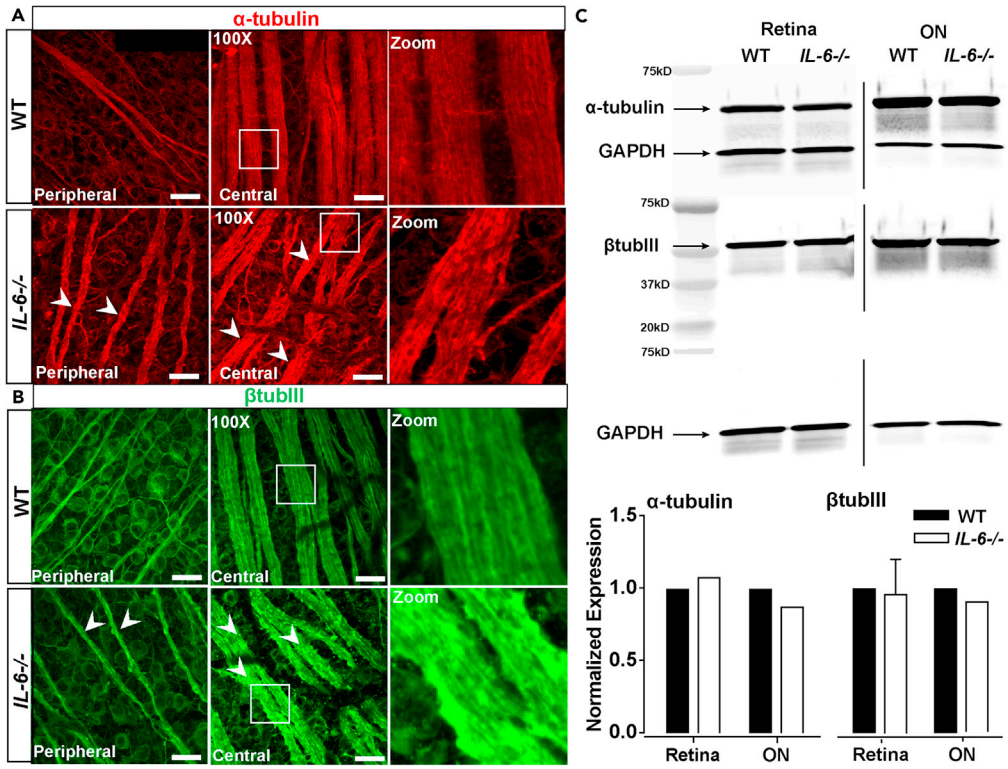

Figure 4. IL-6 deficiency induces tubulin disorganization in RGC axons

(A and B) Representative confocal micrographs (100X) of α-tubulin (A; red) and β-tubulin (βTubIII; B; green) immunolabeling in peripheral (left) and central (middle) regions of wholemount retina from WT (top) and *IL-6−/−* (bottom) mice. Arrowheads indicate regions with aggregated labeling. Boxed regions were zoomed to highlight aggregations (right). Scale = 20 μm.

(C) Immunoblotting (top) and densitometric quantification (bottom) of α-tubulin (50 kDa) and β-tubulin (55 kDa) normalized to GAPDH (36 kDa) in retina and optic nerve from WT and *IL-6−/−* mice (n = 3). Error bars = standard deviation.

β-tubulin. PLA is designed to identify protein complexes *in situ* (Söderberg et al., 2006). In PLA, a fluorescent signal is obtained when the target proteins are localized within 40nm of each other (Söderberg et al., 2006). Thus, this assay detects protein co-localization at single-molecule resolution *in situ*, which is highly suggestive of protein-protein interaction (Söderberg et al., 2006; Debaize et al., 2017; Sable et al., 2018). Accordingly, previous studies indicate that proteins identified as co-localized by immunohistochemistry do not necessarily meet the criteria to produce a PLA signal (Lutz et al., 2017). Our PLA studies revealed that MAP2:β-tubulin interactions were surprising low, even in WT optic nerve (Figure S2). Even so, *IL-6−/−* optic nerve exhibited no fluorescent puncta above background levels observed in no antibody controls (Figure S2). These data suggest that the absence of IL-6 signaling likely perturbs the relatively weak interactions between β-tubulin and MAP2 in optic nerve.

MAP2 is only one of many proteins in the large scaffold of microtubule tertiary and quaternary structure. Thus, we examined another candidate MAP with established links to both tubulin stability and IL-6 signaling. Stathmin interacts with and binds to tubulin dimers to facilitate microtubule depolymerization (Belmont and Mitchison, 1996; Curmi et al., 1997; Ng et al., 2006). Stathmin itself can also interact with STAT3 protein, which is most widely appreciated as the primary transcription factor downstream of IL-6 (Bromberg and Darnell, 2000). RNA sequencing revealed no difference in gene transcription for either *Stat3* or *stathmin* in WT versus *IL-6−/−* retina (Table 1). Similarly, immunohistochemical labeling against Stathmin and STAT3 in optic nerve sections revealed qualitatively similar localization and expression patterns in WT and *IL-6−/−* mice (Figure 6A). To determine whether STAT3 and stathmin are localized closely enough to interact in optic nerve, we performed PLA against STAT3 and stathmin in optic nerve sections from WT and *IL-6−/−* mice. In WT optic nerve, STAT-3:stathmin PLA revealed fluorescent puncta

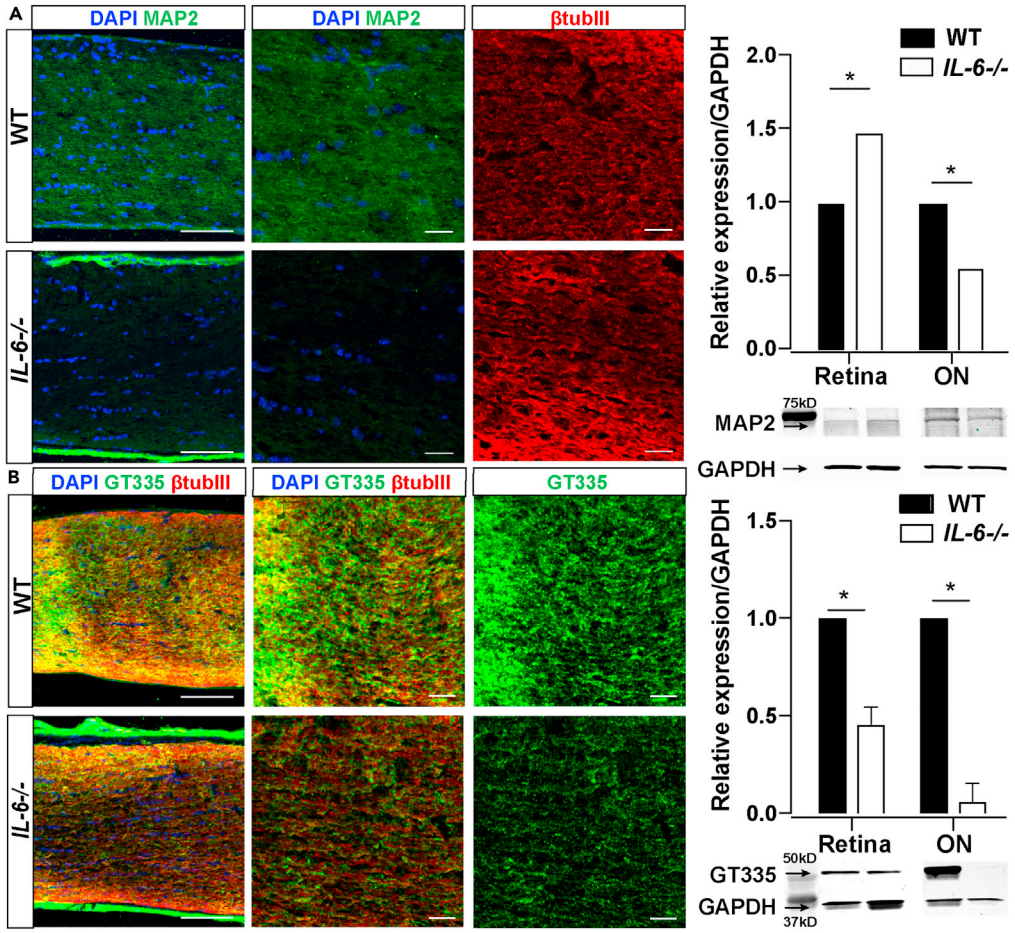

Figure 5. IL-6 deficiency dramatically reduces MAP2 localization and poly-glutamylation of tubulin in optic nerve

(A) Left Panels: Representative confocal images of MAP2 (green) and β-III-tubulin (red) immunolabeling with DAPI counterstain (blue) in cryosections of optic nerve from WT and *IL6−/−* mice. Scale = 40 μm, left panel and 20μm, middle and right panels. Right Panels: Immunoblotting (bottom) and densitometric quantification (top) of MAP2 (70 kDa) normalized to GAPDH (36 kDa) in retina and optic nerve from WT and *IL-6−/−* mice (n = 3). Error bars = standard deviation. Asterisks = $p \leq 0.01$.

(B) Left Panels: Representative confocal images of polyglutamylated tubulin (GT335; green) and β-III-tubulin (red) immunolabeling with DAPI counterstain (blue) in cryosections of optic nerve from WT and *IL6−/−* mice. Scale = 40 μm, left panel and 20μm, middle and right panels. Right Panels: Immunoblotting (bottom) and densitometric quantification (top) of GT335 normalized to GAPDH in retina and optic nerve from WT and *IL-6−/−* mice (n = 3). Error bars = standard deviation. Asterisks = $p \leq 0.01$.

throughout RGC axons, indicating that STAT-3 and stathmin localize within 40nm of each other (Figure 6B). In contrast, *IL-6−/−* optic nerve exhibited minimal fluorescent puncta (Figure 6B) that was similar to no antibody controls (Figure 6B). These data suggest that: (1) STAT3 and stathmin co-localize with one another in optic nerve and (2) this association is close enough to interact directly as part of a cytoskeletal protein complex in RGCs.

To further examine the potential interaction between STAT3 and stathmin in RGC axons, we first determined whether the STAT3-stathmin association was a conserved element of RGC axo-architecture. In optic nerve sections from swine, we examined STAT3 and stathmin by PLA. These PLA studies revealed fluorescent puncta throughout RGC axon bundles that was similar to that observed in mice (Figures 6B and 6C). Western blotting in whole protein lysate confirmed the presence of both STAT3 and stathmin in porcine optic nerve (Figure 6D). Densitometry analysis relative to GAPDH expression suggested that STAT3 protein (0.782 O.D. ± 0.05 O.D.) is present at a higher concentration than stathmin (0.155 O.D. ± 0.06 O.D.) in

Table 1. IL-6 deficiency does not alter STAT3 or stathmin gene expression

Gene	Function	log2 fold change	p value
Stat3	Signal Transducer and Activator of Transcription 3	−0.03	0.70641
Stmn1	Stathmin-1	0.05	0.39545

porcine optic nerve ($p<0.001$). This is consistent with the qualitative difference in the intensity of STAT3 and stathmin immunolabeling in mouse optic nerve (Figure 6A).

To determine whether the positive PLA signal observed in mouse and porcine optic nerves arises from direct interaction between STAT3 and stathmin, we performed co-immunoprecipitation (Co-IP) in porcine optic nerves. We utilized anti-stathmin antibody conjugated to Protein A-coated beads to precipitate stathmin and its binding partners from whole protein lysates of the porcine optic nerve. Stathmin IP samples were then probed by Western blotting for the presence of STAT3. Protein A-only IP samples served as the negative control. These Co-IP studies revealed the presence of STAT3 in stathmin IP samples, but not in the Protein A IP control samples (Figure 6E). Unfortunately, the low level of stathmin expression in optic nerve, combined with its small molecular weight (17 kDa), proved challenging for reverse co-IP. However, the positive detection of this interaction by both *in situ* (PLA) and biochemical (Co-IP) modalities, strongly suggest that: (1) STAT3 protein interacts with stathmin in RGC axons and (2) this interaction is likely dependent upon IL-6.

IL-6 activation promotes interactions between STAT3 and stathmin in RGCs

To determine whether IL-6 alters the localization and expression patterns of STAT3 and stathmin directly in RGCs, we treated primary cultures of purified RGCs with recombinant IL-6 (rIL6; 1ng/mL or 10ng/mL) for 4 days and examined STAT3 and stathmin expression by immunocytochemistry. IL-6-dependency was confirmed by reversal with the addition of 10ng/mL neutralizing IL-6 antibody (nAb). The highest intensity labeling was noted in the soma for all conditions (Figure S3). However, treatment with rIL-6 appeared to impact the localization of STAT3 and stathmin in RGC neurites (Figures S3A and S3B). To attempt capture of these changes in localization, we masked RGC soma and measured the intensity of STAT3 and stathmin immunolabeling in neurites only. Treatment with 10ng/mL rIL-6, but not 1ng/mL rIL-6, increased the labeling intensity for STAT3 in RGC neurites by 45% ($p>0.05$ and $p = 0.04$, respectively; Figure S3A and S3C). Co-administration of 1ng/mLnAb and 10ng/mL rIL-6 prevented this increase in STAT3 intensity ($p>0.05$; Figure S3A and S3C). While quantification revealed no significant difference in the integrated pixel density (Figure S3C), aggregates of stathmin were visible in RGC neurites following treatment with 10ng/mL rIL-6 (Figure S3B). These aggregations were not visible when IL-6 nAb was co-administered with the 10ng/mL rIL-6 (Figure S3B).

Using the same pharmacological paradigm above, we determined whether IL-6 promotes interaction between STAT3 and stathmin, using PLA. PLA against STAT3:Stathmin revealed that rIL-6 treatment increases interactions between these two proteins, particularly in RGC neurites (Figure 7A). This was most notable with the highest dose of rIL-6 and was reversed by addition of nAb. Subcellular changes in localization are more easily visualized with 3D mapping of thermal luts for PLA signal (Figures 7A and 7B). To quantify IL-6-induced changes in STAT3-statmin interaction, we measured the integrated density of PLA fluorescence (Figure 7C). Like STAT3 and stathmin immunolabeling, changes in neurite localization appeared to be particularly significant. Thus, we masked RGC soma for measurement and calculation of PLA integrated density. These analyses revealed that 10ng/mL rIL-6 increases PLA signal intensity in RGC neurites by 24% over control conditions ($p<0.01$; Figure 7C). Co-treatment with 10ng/mL rIL-6 and IL-6 nAb prevented this change in PLA signal, as compared to 10ng/mL rIL-6 alone ($p<0.01$; Figure 7C). PLA signal in the presence of vehicle and 10ng/mL rIL-6 + 10ng/mL IL-6 nAb were identical ($p = 0.982$; Figure 7C). Together, these data indicate that IL-6 directly promotes interaction between STAT3 and stathmin in RGC processes.

IL-6-mediated effects on microtubule structure influences stabilization and destabilization dynamics

To identify the functional consequence of IL-6-mediated STAT3 activation on microtubule behavior, we challenged RGCs with the microtubule destabilizer colchicine. Microtubule destabilization by colchicine

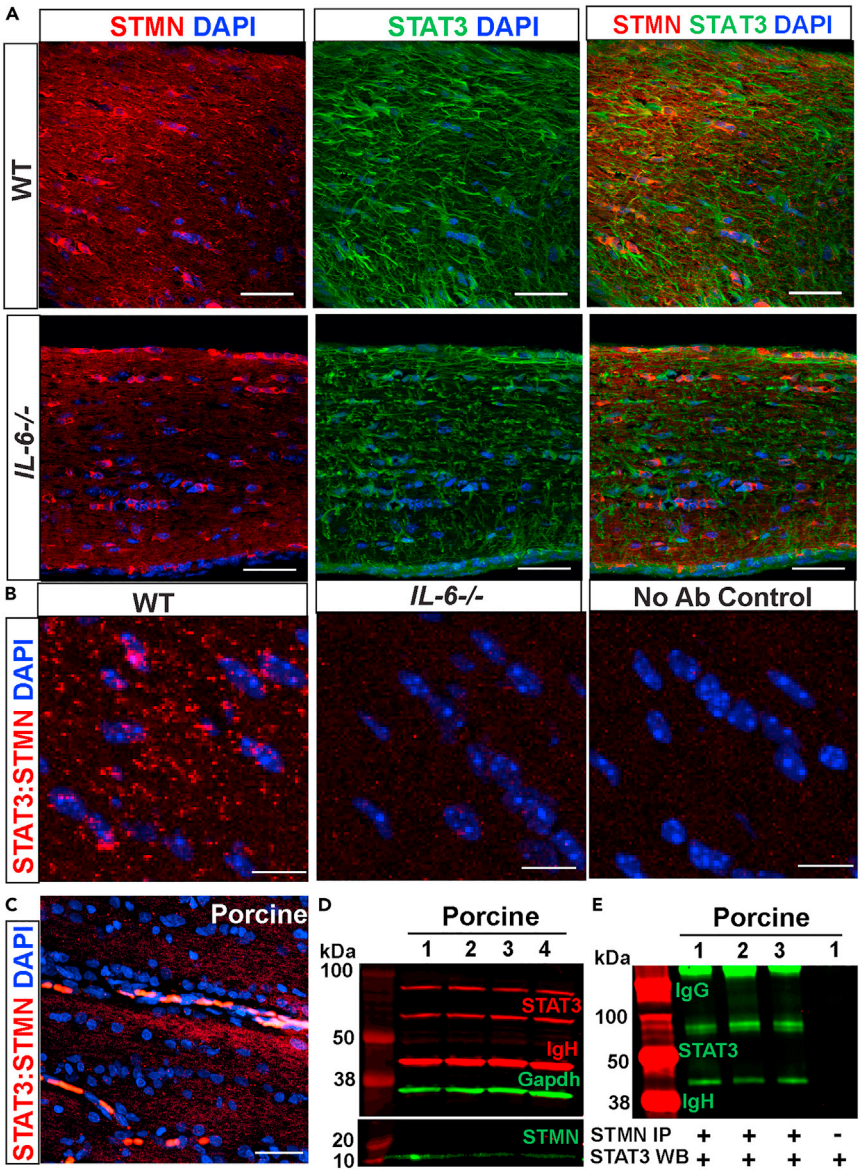

Figure 6. IL-6 deficiency inhibits STAT3:Stathmin protein–protein interactions

(A) Representative 60X confocal images of co-immunolabeling against stathmin (STMN, red) and STAT3 (green) with DAPI counterstain (blue) in cryosections of optic nerve from WT and *IL6−/−* mice. Scale = 40 μm.

(B) Representative confocal micrographs (60X) of STAT3:STMN PLA (red puncta) and no antibody control (bottom; WT only) with DAPI counterstain (blue) in cryosections of optic nerve from WT (top) and *IL-6−/−* (middle) mice. Scale = 10 μm.

(C) Representative confocal micrograph (60X) of STAT3:STMN PLA (red puncta) with DAPI counterstain (blue) in cryosections of porcine optic nerve. Scale = 40 μm.

(D) Representative immunoblot against STAT3 (79–86 kDa), stathmin (17 kDa) and GAPDH (37 kDa) in whole protein lysates from porcine optic nerve.

(E) Representative immunoblot against STAT3 in porcine optic nerve following co-immunoprecipitation in whole protein lysates with anti-stathmin antibody (left) or Protein A beads alone (right).

ultimately leads to neuronal cell death with prolonged exposure (Gibbs et al., 1980; Emons et al., 1990). To assess changes in the integrity of β-tubulin+ neurites prior to cell death and to separate STAT3 protein and transcriptional mechanisms, we utilized a short experimental period of 2 h. Primary cultures of purified RGCs were treated with 1mM colchicine (Gibbs et al., 1980; Emons et al., 1990) for 1 h with or without 1 h of pre-treatment with 1ng/mL rIL-6. We confirmed specificity of our IL-6-dependent outcomes with a

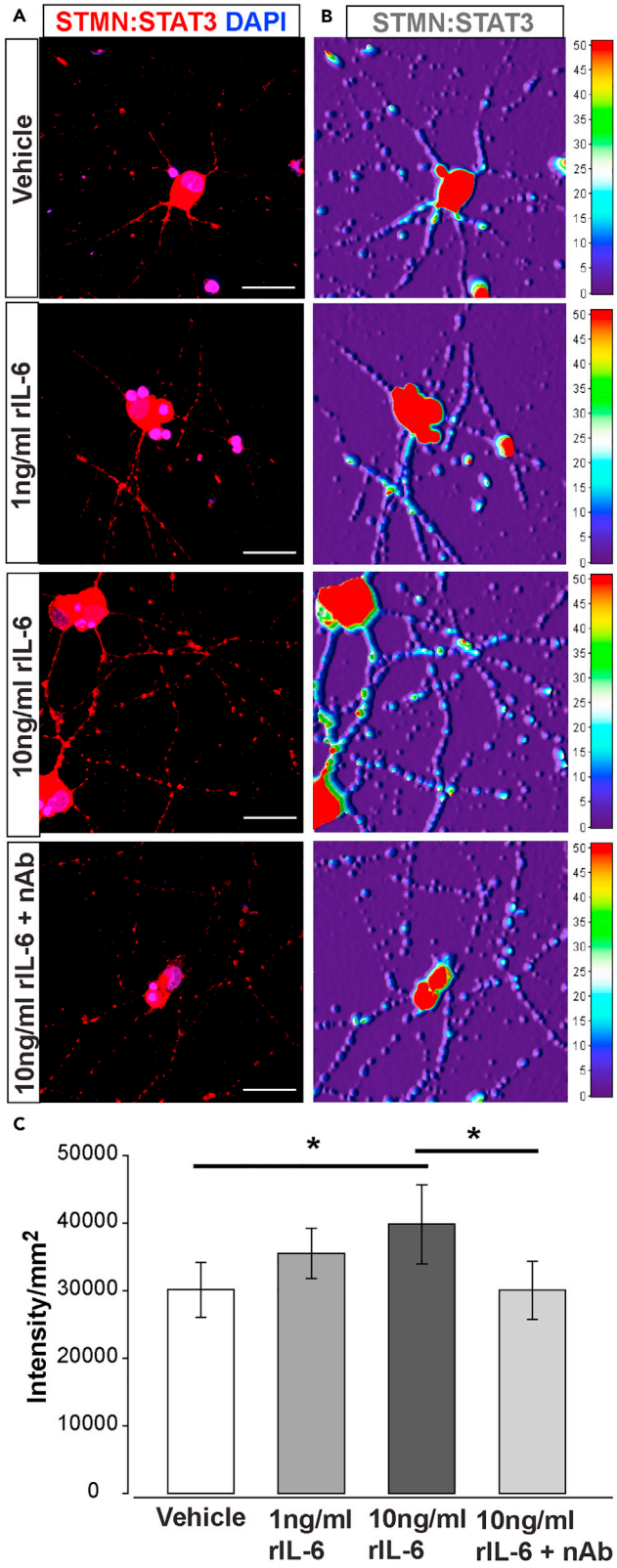
A
STMN:STAT3 DAPI
B
STMN:STAT3
Vehicle
1ng/ml rIL-6
10ng/ml rIL-6
10ng/ml rIL-6 + nAb
50
45
40
35
30
25
20
15
10
5
0
C
*
*
Intensity/mm2
50000
40000
30000
20000
10000
0
Vehicle
1ng/ml rIL-6
10ng/ml rIL-6
10ng/ml rIL-6 + nAb

Figure 7. IL-6 directly promotes STAT3 and stathmin interaction in RGCs

(A) Representative confocal micrographs (100X) of STAT3:STMN PLA (red puncta) with DAPI counterstain (blue) in purified, primary RGCs following 4-day treatment with vehicle, recombinant IL-6 (rIL-6; 1ng/mL and 10ng/mL) or 10ng/mL rIL-6 + neutralizing antibody (nAb). Scale = 20 μm.

(B) 3D plots of thermal luts for STAT3:STMN PLA signal in each micrograph pictured in (A). Thermal scale is 0 (purple) to 50 (red).

(C) Quantification of PLA signal present in RGC neurites only. PLA signal is represented as integrated density/mm^2 (y-axis) for each treatment condition. Asterisks indicate $p<0.05$. Error bars represent standard deviation.

nAb (10ng/mL) co-administration. To quantify microtubule stabilization, we immunolabeled RGCs with antibodies against β-tubulin (Figure 8A) and performed Scholl analysis measuring the number of intersections between β-tubulin+ neurites and Scholl radius intervals originating from the center of RGC soma (Figures 8B and 8C). The Scholl intersection profile (SIP) for each cell was quantified as area under this curve (AUC; Figure 8D). Treatment with 1mM colchicine reduced the SIP by 67%, as compared to control ($p<0.001$; Figure 8D). Pre-treatment with 1ng/mL rIL-6 alone did not alter the SIP, as compared to control ($p = 0.25$; Figure 8D). However, pre-treatment with 1ng/mL rIL-6 prevented colchicine-induced reductions in SIP ($p<0.001$ versus colchicine alone; $p>0.05$ versus control or rIL-6 alone; Figure 8D). This preservative effect was successfully reversed by co-administration of nAb against IL-6 ($p<0.001$ versus control or rIL-6 alone or rIL-6 + colchicine; $p>0.05$ versus colchicine alone; Figure 8D).

We further refined our assessment of neurite outcomes by examining two components of the SIP – the maximum number of intersections and the radius at which this maximum occurred. We found that the maximum number of intersections achieved by β-tubulin+ neurites did not change with IL-6 or colchicine treatments ($p>0.05$ for all; Figure 8E). However, the radius distance at which this maximum occurred was 52–65% lower for RGCs treated with either colchicine alone or colchicine + rIL-6 pre-treatment + nAb, as compared to control, rIL-6 alone and colchicine + rIL-6 pre-treatment ($p<0.02$ for all; Figure 8F). Together, these data suggest that IL-6 is sufficient to prevent microtubule destabilization and preserve neurite structure.

DISCUSSION

IL-6 is well-established as an inflammatory mediator, but recent research indicates that IL-6 is a multifunctional, neuropoetic factor with crucial roles in the CNS (Wagner, 1996). These non-inflammatory functions include axon regeneration (Leibinger et al., 2013;Yang and Tang, 2017), neurogenesis (Marz et al., 1997; Schafer et al., 1999; Sappington et al., 2006; Chidlow et al., 2012;Leibinger et al., 2013), and neurotrophic activities (Kahn and De Vellis, 1994; Marz et al., 1997; Schafer et al., 1999; Thier et al., 1999; Sulistio et al., 2018). A large proportion of the neuropoetic activities for IL-6 involve axon growth and repair (Hirota et al., 1996; Zhong et al., 1999; Cafferty et al., 2004). Here we describe, for the first time, a potential mechanism underlying neurotrophic activities of IL-6 relating to axons. Using *in vivo* and *in vitro* models, we describe a role for IL-6 signaling in the modulation of microtubule dynamics within CNS axons that is mediated by STAT3 protein-protein interactions with microtubules and MAPs.

Our data demonstrate that IL-6 deficiency reduces the rate of anterograde axon transport in the optic projection (Figure 1). This delay in axonal transport is not due to decreased density of RGCs or improper RGC termination in the brain (Figure 2). Rather, IL-6 deficiency resulted in ultrastructural abnormalities of axon microtubules (Figure 3). Examination of β-tubulin and α-tubulin revealed a disorganized pattern of localization that was not accompanied by changes in overall protein expression (Figure 4). Axon diameter is mostly associated with neurofilaments (Leterrier et al., 1996). However, microtubule structure is the primary mediator of axon diameter in small caliber axons as well as neurofilament-rich axons via mechanisms of cross-linking (Friede and Samorajs, 1970; Gotow et al., 1994). Furthermore, microtubule phenotypes can be linked to axon transport facility directly through motor protein binding and microtubule structure as well as indirectly through interactions with other cyto-skeletal elements, i.e., neuro-filaments (Bulinski et al., 1987; Kreitzer et al., 1999; Andersen, 2000; Tran et al., 2007). Together, these data suggest that microtubule abnormalities are reflected by disorderly arrangement of tubulin rather than changes in overall availability of tubulin and that this finding is likely related to the observed delay in axon transport.

Post-translational modifications (PTMs), including acetylation, phosphorylation, glycylation and tyrosination, play a significant role in establishing interactions among components of axon transport machinery and, thus, on the efficiency of axon transport (Janke, 2014; Sirajuddin et al., 2014;

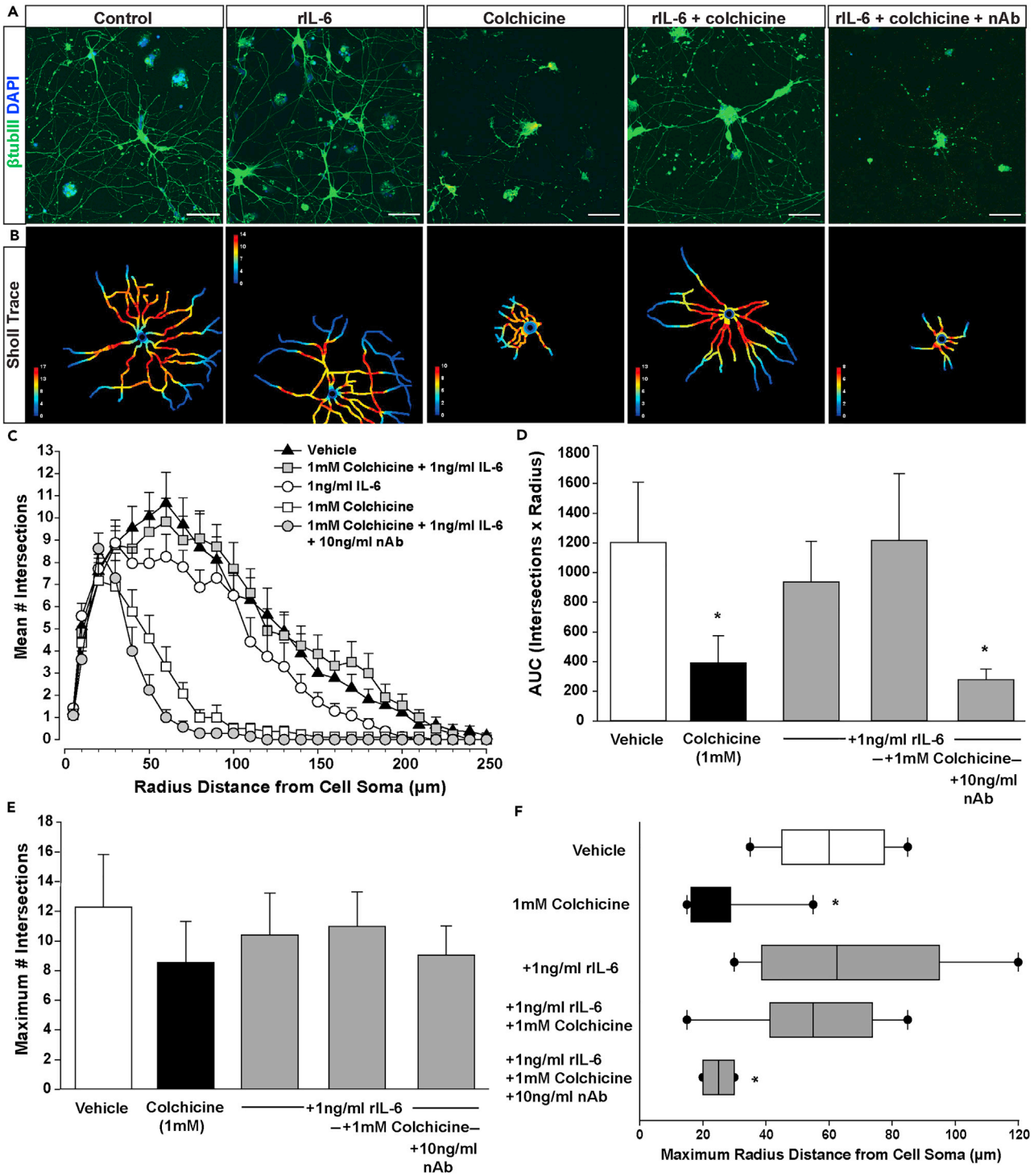

Figure 8. IL-6 stabilizes microtubules and preserves neurite structure

(A) Representative confocal images (40X) of β-III-Tubulin immunolabeling (green) and DAPI counterstain (blue) in primary, purified RGCs treated for 1 h with vehicle or 1mM colchicine following 1 h pre-treatment with vehicle, 1ng/mL rIL-6 or 1ng/mL rIL-6 + 10ng/mL nAb. Scale = 50 μm.

(B) Corresponding Scholl analysis tracings to RGCs pictured in (A).

(C) Scholl function depicting the mean number of intersections between β-tubulin+ neurites and Scholl radius intervals originating from the center of RGC soma for each condition.

Figure 8. *Continued*

(D) Scholl intersection profile (SIP) quantified as the mean area under the curve (AUC) for each condition. Asterisk = $p<0.001$, as compared to vehicle, 1ng/mL rIL-6 and 1ng/mL rIL-6 + 1mM colchicine. Error bars = standard deviation. $n \geq 5$ RGCs per condition.

(E) Quantification of the maximum number of intersections depicted as the mean $\pm$ standard deviation. $n \geq 5$ RGCs per condition. Error bars = standard deviation.

(F) Quantification of the radius distance at which the maximum number of intersections occurred depicted as mean $\pm$ standard deviation. Asterisk = $p<0.05$, as compared to vehicle, 1ng/mL rIL-6 and 1ng/mL rIL-6 + 1mM colchicine. $n \geq 5$ RGCs per condition. Error bars = 95% confidence interval.

Bodakuntla et al., 2020). Microtubule structure and function is influenced by post-translational modifications on tubulin, including acetylation, phosphorylation, glycylation and tyrosination (Janke, 2014; Sirajuddin et al., 2014). Polyglutamylation of tubulin is particularly enriched on neuronal microtubules (Janke and Bulinski, 2011) and is important in fine-tuning MAP and motor protein association with axons (reviewed in Magiera et al., 2018). We found that polyglutamylation of tubulin is nearly undetectable in RGC axons from *IL-6−/−* mice. MAP2 binding to tubulin is proportional to levels of polyglutamylation of tubulin (Boucher et al., 1994; Bonnet et al., 2001). Consistent with the levels of polyglutamylated tubulin, we found negligible localization of MAP2 to RGC axons in *IL-6−/−* mice (Figures 5 and S2). While the reduction in polyglutamylation of tubulin was most dramatic in the optic nerve, the retina of *IL-6−/−* mice also exhibited a reduction in polyglutamylation (Figure 5). In contrast, MAP2 expression was higher in retina from *IL-6−/−* mice than that in WT mice (Figure 5). This suggests that MAP2 protein is "sequestered" in RGC soma rather than being trafficked to RGC axon for association with microtubules. Thus, IL-6 influences microtubule structure at a level that impacts both post-translational modification of the tubulin building blocks and trafficking/association of proteins essential for establishing tertiary and quaternary structure.

Downstream activities of IL-6 are most often linked to STAT3-mediated gene transcription (Magiera et al., 2018). However, STAT3 is also associated with microtubule assemblies in non-neuronal cells, i.e., cancer cells and T-cells (Bonnet et al., 2001; Ng et al., 2006; Kaur et al., 2020). In this context, STAT3 binds stathmin, which is also further associated with MAP2 binding and poly-glutamylation states (Bonnet et al., 2001). In neuronal cells, STAT3 and stathmin are also linked to motor neuron degeneration and dysfunction (Verma et al., 2009; Selvaraj et al., 2012). Accordingly, we assessed STAT3 and stathmin localization and their putative interactions in RGC axons of the optic nerve, using PLA and Co-IP. Our PLA data strongly suggested that STAT3 and stathmin interact in RGC axons within the optic nerve of WT mice and swine (Figure 6). In *IL-6−/−* mice, this STAT3:Stathmin association was completely absent (Figure 6). Western blot and Co-IP studies in swine confirmed direct interaction between stathmin and STAT3 in optic nerve (Figure 6). Inversely, recombinant IL-6 increased STAT3 and stathmin interactions in neurites of primary RGCs purified from rat retina (Figure 7). These data suggest that: (1) STAT3 and stathmin interact in RGC axons, (2) this interaction is conserved between species, (3) IL-6 signaling is required for STAT3-stathmin interaction in RGC axons, and (4) this IL-6 dependency is intrinsic to RGCs and species independent.

In addition to promoting STAT3-stathmin interactions, recombinant IL-6 also prevented colchicine-induced decreases in neurite integrity (Figure 8). Recombinant IL-6 was sufficient to prevent colchicine-induced disruption of neurites. Given our 2-h experimental paradigm, these data indicate that IL-6 is a mediator of microtubule stability via mechanisms that are likely dependent upon protein-protein interactions rather than gene transcription. This is consistent with the established role of STAT3-stathmin interactions in mediating microtubule stability in malignant cells (Ohkawa et al., 2007). Taxol chemotherapy agents (e.g., paclitaxel) destabilize microtubules by decreasing STAT3 binding to stathmin (Selvaraj et al., 2012). This leads to a feedback inhibition loop that further reduces STAT3 activation and STAT3-stathmin interactions to inhibit tumor growth (Sangrajrang et al., 1998; Gao and Bromberg, 2006). Interestingly, resistance to this class of chemotherapeutics is linked to increased polyglutamylation of microtubules, which stabilizes microtubules to counteract microtubule-destabilizing agents (Sangrajrang et al., 1998). Similarly, STAT3-stathmin interactions control microtubule dynamics in migrating T-cells (Verma et al., 2009).

Our data indicate associative relationships between IL-6 signaling, STAT3-stathmin protein interactions and poly-glutamylation of tubulin that mediate microtubule stability. What we do not yet understand is the temporal relationship between these mechanistic elements. Our *in vitro* data suggest rapid modulation of microtubule stability that supports an early, functional response mediated at the protein level. IL-6-dependent changes in MAP2 localization and polyglutamylation of tubulin mirror one another, suggesting a mechanistic link between these two modalities of microtubule structure. However, it is unclear whether

MAP2 trafficking to axons is dependent on polyglutamylation of tubulin or vice versa. Similarly, it is possible that MAP2 and polyglutamylation pathways share a common mediator also impacted by STAT3-stathmin interactions and IL-6 signaling. In any case, our *in vitro* data indicate that IL-6 signaling and downstream effectors intrinsic to RGCs themselves are sufficient to modulate microtubule stability.

Our data elucidate a role for IL-6 in mediating microtubule dynamics via STAT3 protein-protein interactions with MAPs that are further associated with poly-glutamylation of tubulin. STAT3-stathmin interactions and polyglutamylation of tubulin are both associated with stabilization of microtubules in malignant cells and STAT3-stathmin interactions mediate microtubule dynamics in migrating T cells. Our data suggest that these interactions perform a similar role and are IL-6-dependent in healthy RGC axons. These data provide a novel mechanism for neuropoietic activities of IL-6 related to axon development, regeneration and repair.

Limitations of the study

The primary limitations of our study are two-fold. First, the low molecular weight and relative low abundance of stathmin presented a challenge for resolution of the protein by SDS-PAGE. While we were able to overcome this technical hurdle in whole protein samples, it proved insurmountable for bidirectional co-IP, even in porcine optic nerve. This is likely due to both the resolution of low molecular weight and the low protein abundance, which is reduced even further by affinity-based approaches, such as co-IP. To offset this limitation, we demonstrated interaction via two methods, co-IP and PLA, and in two different species, mouse and swine. Second, our intention was to present co-IP validation of disruptions in STAT3 and stathmin interactions in optic nerve from both WT and *IL-6−/−* mice. Our colony of *IL-6−/−* mice was lost during COVID prior to completion of the co-IP experiments. Unfortunately, the live repository of *IL-6−/−* mice at Jackson Laboratories was transitioned to a C57Bl/6 background. The time and financial cost of either cryorecovery for the *IL-6−/−* background or repetition of our experiments for consistency of genetic background were beyond our capacity. Future studies could be performed to validate dependency of STAT-stathmin interactions on IL-6 signaling, utilizing the new *IL-6−/−* strain or an alternative perturbation of IL-6 signaling.

STAR★METHODS

Detailed methods are provided in the online version of this paper and include the following:

- KEY RESOURCES TABLE
- RESOURCE AVAILABILITY
  - Lead contact
  - Materials availability
  - Data and code availability
- EXPERIMENTAL MODELS AND SUBJECT DETAILS
  - Animals
  - Primary cell culture
- METHOD DETAILS
  - Tissue preparation
  - Anterograde axon transport measurements
  - Immunohistochemistry
  - Epon embedding and electron microscopy
  - RNA-Seq
  - Proximity ligation assay
  - Immunoblotting
  - Co-Immunoprecipitation
- QUANTIFICATION AND STATISTICAL ANALYSIS
  - Quantification of RGC soma and axons
  - Protein concentration
  - PLAsignal intensity
  - Scholl analysis
  - Statistics

SUPPLEMENTAL INFORMATION

Supplemental information can be found online at https://doi.org/10.1016/j.isci.2021.103141.

ACKNOWLEDGMENTS

These studies were supported by funding from: (1) National Eye Institute - RO1EY020496 (RMS) and P30EY08126 (Vanderbilt Vision Research Center) and (2) Research to Prevent Blindness, Inc. - Unrestricted Grant (Vanderbilt Eye Institute) and Career Development Award (RMS). The authors would like to thank the Vanderbilt University Medical Center Cell Imaging Shared Resource for confocal imaging and electron microscopy. The authors would also like to thank Dr. James Jordan in the Department of Surgical Sciences – Cardiothoracic Surgery at Wake Forest School of Medicine for donating swine tissue. Finally, the authors thank Joanne Konstantopoulos in the Department of Neurobiology and Anatomy for technical assistance in the preparation of swine tissue.

AUTHOR CONTRIBUTIONS

Conceptualization (LKW, FDE, RMS), Formal Analysis (LKW, FDE, RMS, JLS, DOK), Investigation (LKW, FDE, GD, CRF, PS, PJG, JLS, DOK, JRG), Visualization (LKW, FDE, JRG, RMS), Validation (LKW, FDE, RMS), Writing – Original Draft (LKW, FDE, RMS), Writing – Revising and Editing (LKW, FDE, RMS), Supervision (RMS), Project Administration (RMS), Funding Acquisition (RMS)

DECLARATION OF INTERESTS

The authors declare no competing interests.

INCLUSION AND DIVERSITY

We worked to ensure sex balance in the selection of non-human subjects. One or more of the authors of this paper self-identifies as an underrepresented ethnic minority in science. One or more of the authors of this paper received support from a program designed to increase minority representation in science.

Received: August 28, 2020
Revised: June 2, 2021
Accepted: September 14, 2021
Published: October 22, 2021

REFERENCES

Abbott, C.J., Choe, T.E., Lusardi, T.A., Burgoyne, C.F., Wang, L., and Fortune, B. (2013). Imaging axonal transport in the rat visual pathway. Biomed. Opt. Express. *4*, 364–386.

Al-Bassam, J., Ozer, R.S., Safer, D., Halpain, S., and Milligan, R.A. (2002). MAP2 and tau bind longitudinally along the outer ridges of microtubule protofilaments. J. Cell Biol. *157*, 1187–1196.

Andersen, S.S. (2000). Spindle assembly and the art of regulating microtubule dynamics by MAPs and Stathmin/Op18. Trends Cell Biol *10*, 261–267.

Baran, P., Hansen, S., Waetzig, G.H., Akbarzadeh, M., Lamertz, L., Huber, H.J., Ahmadian, M.R., Moll, J.M., and Scheller, J. (2018). The balance of interleukin (IL)-6, IL-6soluble IL-6 receptor (sIL-6R), and IL-6sIL-6Rsgp130 complexes allows simultaneous classic and trans-signaling. J. Biol.Chem. *293*, 6762–6775.

Bauer, S., Kerr, B.J., and Patterson, P.H. (2007). The neuropoietic cytokine family in development, plasticity, disease and injury. Nat. Rev. Neurosci. *8*, 221–232.

Belmont, L.D., and Mitchison, T.J. (1996). Identification of a protein that interacts with tubulin dimers and increases the catastrophe rate of microtubules. Cell *84*, 623–631.

Bird, A.D., and Cuntz, H. (2019). Dissecting Sholl analysis into its functional components. Cell Rep. *27*, 3081–3096.

Bodakuntla, S., Schnitzler, A., Villablanca, C., Gonzalez-Billault, C., Bieche, I., Janke, C., and Magiera, M.M. (2020). Tubulin polyglutamylation is a general traffic-control mechanism in hippocampal neurons. J.CellSci. *133*, 241802.

Bonnet, C., Boucher, D., Lazereg, S., Pedrotti, B., Islam, K., Denoule, P., and Larcher, J.C. (2001). Differential binding regulation of microtubule-associated proteins MAP1A, MAP1B, and MAP2 by tubulin polyglutamylation. J. Biol.Chem. *276*, 12839–12848.

Borsini, A., Zunszain, P.A., Thuret, S., and Pariante, C.M. (2015). The role of inflammatory cytokines as key modulators of neurogenesis. Trends Neurosci. *38*, 145–157.

Boucher, D., Larcher, J.C., Gros, F., and Denoulet, P. (1994). Polyglutamylation of tubulin as a progressive regulator of in vitro interactions between the microtubule-associated protein Tau and tubulin. Biochemistry *33*, 12471–12477.

Bromberg, J., and Darnell, J.E., Jr. (2000). The role of STATs in transcriptional control and their impact on cellular function. Oncogene *19*, 2468–2473.

Bulinski, J.C., Gundersen, G.C., and Webster, D.R. (1987). A function for tubulin tyrosination? Nature *328*, 676.

Cafferty, W.B., Gardiner, N.J., Das, P., Qiu, J., McMahon, S.B., and Thompson, S.W. (2004). Conditioning injury-induced spinal axon regeneration fails in interleukin-6 knock-out mice. J. Neurosci. *24*, 4432–4443.

Chidlow, G., Wood, J.P., Ebneter, A., and Casson, R.J. (2012). Interleukin-6 is an efficacious marker of axonal transport disruption during experimental glaucoma and stimulates neuritogenesis in cultured retinal ganglion cells. Neurobiol. Dis. *48*, 568–581.

Crish, S.D., Sappington, R.M., Inman, D.M., Horner, P.J., and Calkins, D.J. (2010). Distal axonopathy with structural persistence in glaucomatous neurodegeneration. Proc. Natl. Acad. Sci. U.S.A. *107*, 5196–5201.

Curmi, P.A., Andersen, S.S., Lachkar, S., Gavet, O., Karsenti, E., Knossow, M., and Sobel, A. (1997). The stathmin/tubulin interaction in vitro. J. Biol. Chem. *272*, 25029–25036.

Debaize, L., Jakobczyk, H., Rio, A.-G., Gandemer, V., and Troade, M.-B. (2017). Optimization of proximity ligation assay (PLA) for detection of protein interactions and fusion proteins in non-adherent cells: application to pre-B lymphocytes. Mol. Cytogenet. *10*, 27.

Dehmelt, L., and Halpain, S. (2005). The MAP2/Tau family of microtubule-associated proteins. Genome Biol. *6*, 204.

Dreher, B., Sefton, A.J., Ni, S.Y., and Nisbett, G. (1985). The morphology, number, distribution and central projections of Class I retinal ganglion cells in albino and hooded rats. Brain Behav.Evol. *26*, 10–48.

Duncan, D.S., McLaughlin, W.M., Vasilakes, N., Echevarria, F.D., Formichella, C.R., and Sappington, R.M. (2017). Characterization of constitutive and stress-induced Ccl5 signaling in rodent retina. J. Clin. Cell.Immunol. *8*, 506.

Duncan, D.S., Weiner, R.L., Weitlauf, C., Risner, M.L., Roux, A.L., Sanford, E.R., Formichella, C.R., and Sappington, R.M. (2018). Ccl5 mediates proper wiring of feedforward and lateral inhibition pathways in the inner retina. Front. Neurosci. *1*, 702.

Echevarria, F.D., Formichella, C.R., and Sappington, R.M. (2017). Interleukin-6 deficiency attenuates retinal ganglion cell axonopathy and glaucoma-related vision loss. Front. Neurosci. *11*, 318.

Emons, A.M.C., Wolters-Arts, A.M.C., Traas, J.A., and Derksen, J. (1990). The effect of colchicine on microtubules and microfibrils in root hairs. Acta Bot. Neerl. *39*, 19–27.

Felgner, H., Frank, R., Biernat, J., Mandelkow, E.M., Mandelkow, E., Ludin, B., Matus, A., and Schliwa, M. (1997). Domains of neuronal microtubule-associated proteins and flexural rigidity of microtubules. J. Cell Biol. *138*, 1067–1075.

Fernandez, D.C., Pasquini, L.A., Dorfman, D., Aldana Marcos, H.J., and Rosenstein, R.E. (2012). Early distal axonopathy of the visual pathway in experimental diabetes. Am. J. Pathol. *180*, 303–313.

Fernando, M.R., Reyes, J.L., Iannuzzi, J., Leung, G., and McKay, D.M. (2014). The pro-inflammatory cytokine, interleukin-6, enhances the polarization of alternatively activated macrophages. PLoS One *9*, e94188.

Ferreira, T., Blackman, A., Oyrer, J., Jayabal, A., Chung, A., Watt, A., Sjöström, J., and van Meyel, D. (2014). Neuronal morphometry directly from bitmap images. Nat. Methods *11*, 982–984.

Fischer, R.A., Risner, M.L., Roux, A.L., Wareham, L.K., and Sappington, R.M. (2019). Impairment of membrane repolarization accompanies axon transport deficits in glaucoma. Front. Neurosci. *13*, 1139.

Fischer, R.A., Zhang, Y., Risner, M.L., Li, D., Xu, Y., and Sappington, R.M. (2018). Impact of graphene on the efficacy of neuron culture substrates. Adv. Healthc.Mater. *7*, 1701290.

Formichella, C., Abella, S.K., Sims, S.M., Cathcart, H.M., and RM Sappington, R.M. (2014). Astrocyte reactivity: abiomarker for ganglion cell health in retinal neurodegeneration. J. Clin. Cell.Immunol. *5*, 15.

Friede, R.L., and Samorajs, T. (1970). Axon caliber related to neurofilaments and microtubules in sciatic nerve fibers of rats and mice. Anat. Rec. *167*, 379–387.

Gao, S.P., and Bromberg, J.F. (2006). Touched and moved by STAT3. Sci. STKE *2006*, pe30.

Gibbs, J.B., Hsu, C.-Y., Terasaki, W.L., and Brooker, G. (1980). Calcium and microtubule dependence for increased ornithine decarboxylase activity stimulated by β3-adrenergic agonists, dibutyryl cyclic AMP, or serum in a rat astrocytoma cell line. Proc. Natl. Acad. Sci. *77*, 995–999.

Gotow, T., Tanaka, T., Nakamura, Y., and Takeda, M. (1994). Dephosphorylation of the largest neurofilament subunit protein influences the structure of crossbridges in reassembled neurofilaments. J. Cell Sci. *107*, 1949–1957.

Hama, T., Miyamoto, M., Tsukui, H., Nishio, C., and Hatanaka, H. (1989). Interleukin-6 as a neurotrophic factor for promoting the survival of cultured basal forebrain cholinergic neurons from postnatal rats. Neurosci.Lett. *104*, 340–344.

Hirano, T., Taga, T., Nakano, N., Yasukawa, K., Kashiwamura, S., Shimizu, K., Nakajima, K., Pyun, K.H., and Kishimoto, T. (1985). Purification to homogeneity and characterization of human B-cell differentiation factor (BCDF or BSFp-2). Proc. Natl. Acad. Sci. U.S.A. *82*, 5490–5494.

Hirokawa, N., Hisanaga, S., and Shiomura, Y. (1988). MAP2 is a component of crossbridges between microtubules and neurofilaments in the neuronal cytoskeleton: quick-freeze, deep-etch immunoelectron microscopy and reconstitution studies. J. Neurosci. *8*, 2769–2779.

Hirota, H., Kiyama, H., Kishimoto, T., and Taga, T. (1996). Accelerated nerve regeneration in mice by upregulated expression of interleukin (IL) 6 and IL-6 receptor after trauma. J. Exp.Med. *183*, 2627–2634.

Janke, C. (2014). The tubulin code: molecular components, readout mechanisms, and functions. J.CellBiol *206*, 461–472.

Janke, C., and Bulinski, J.C. (2011). Post-translational regulation of the microtubule cytoskeleton: mechanisms and functions. Nat. Rev. Mol.Cell Biol *12*, 773–786.

Kahn, M.A., and De Vellis, J. (1994). Regulation of an oligodendrocyte progenitor cell line by the interleukin-6 family of cytokines. Glia *12*, 87–98.

Kapitein, L.C., and Hoogenraad, C.C. (2015). Building the neuronal microtubule cytoskeleton. Neuron *87*, 492–506.

Kaur, S., Bansal, Y., Kumar, R., and Bansal, G. (2020). A Panoramic Review of IL-6: structure, Pathophysiological roles and Inhibitors. Bioorg. Med.Chem. *28*, 115327.

Kreitzer, G., Liao, G., and Gundersen, G.C. (1999). Detyrosination of tubulin regulates the interaction of intermediate filaments with microtubules in vivo via a kinesin-dependent mechanism. Mol. Biol. Cell. *10*, 1105–1118.

Leibinger, M., Müller, A., Gobrecht, P., Diekmann, H., Andreadaki, A., and Fischer, D. (2013). Interleukin-6 contributes to CNS axon regeneration upon inflammatory stimulation. Cell Death Dis *4*, e609.

Leterrier, J.F., Käs, J., Hartwig, J., Vegners, R., and Janmey, P.A. (1996). Mechanical effects of neurofilament cross-bridges.Modulation by phosphorylation, lipids and interactions with F-actin. J. Biol. Chem. *271*, 15687–15694.

Lutz, M.I., Schwaiger, C., Hochreiter, B., Kovacs, G.G., and Schmid, J.A. (2017). Novel approach for accurate tissue-based protein colocalization and proximity microscopy. Sci. Rep. *7*, 2668.

Magiera, M.M., Singh, P., Gadadhar, S., and Janke, C. (2018). Tubulin posttranslational modifications and emerging links to human disease. Cell *173*, 1323–1327.

Margolis, T.P., Marchand, C.M., Kistler, H.B., Jr., and LaVail, L.H. (1981). Uptake and anterograde axonal transport of wheat germ agglutinin from retina to optic tectum in the chick. J. Cell Biol. *89*, 152–156.

Marz, P., Herget, T., Lang, E., Otten, U., and Rose-John, S. (1997). Activation of gp130 by IL-6/soluble IL-6 receptor induces neuronal differentiation. Eur. J. Neurosci. *9*, 2765–2773.

Ng, D.C., Lin, B.H., Lim, C.P., Huang, G., Zhang, T., Poli, V., and Cao, X. (2006). Stat3 regulates microtubules by antagonizing the depolymerization activity of stathmin. J. Cell Biol. *172*, 245–257.

Noma, H., Minamoto, A., Funatsu, H., Tsukamoto, H., Nakano, K., Yamashita, H., and Mishima, H.K. (2006). Intravitreal levels of vascular endothelial growth factor and interleukin-6 are correlated with macular edema in branch retinal vein occlusion. Graefes Arch. Clin. Exp. Ophthalmol. *244*, 309–315.

Noma, H., Funatsu, H., Mimura, T., Harino, S., and Hori, S. (2009). Vitreous levels of interleukin-6 and vascular endothelial growth factor in macular edema with central retinal vein occlusion. Ophthalmology *116*, 87–93.

Ohkawa, N., Hashimoto, K., Hino, T., Migishima, R., Yokoyama, M., Kano, M., and Inokuchi, K. (2007). Motor discoordination of transgenic mice overexpressing a microtubule destabilizer, stathmin, specifically in Purkinje cells. Neurosci. Res. *59*, 93–100.

Sable, R., Jambunathan, N., Singh, S., Pallerla, S., Kousoulas, K.G., and Jois, S. (2018). Proximity ligation assay to study protein–protein interactions of proteins on two different cells. Biotechniques *65*, 149–157.

Sanchez, R.N., Chan, C.K., Garg, S., Kwong, J.M., Wong, M.J., Sadun, A.A., and Lam, T.T. (2003). Interleukin-6 in retinal ischemia reperfusion injury in rats. Invest. Ophthalmol.Vis. Sci. *44*, 4006–4011.

Sangrajrang, S., Denoulet, P., Laing, N.M., Tatoud, R., Millot, G., Calvo, F., Tew, K.D., and Fellous, A. (1998). Association of estramustine resistance in human prostatic carcinoma cells with modified patterns of tubulin expression. Biochem. Pharmacol. *55*, 325–331.

Sappington, R.M., Chan, M., and Calkins, D.J. (2006). Interleukin-6 protects retinal ganglion cells from pressure-induced death. Invest. Ophthalmol.Vis. Sci. *47*, 2932–2942.

Sappington, R.M., Pearce, D.A., and Calkins, D.J. (2003). Optic nerve pathology in a murine model of juvenile neuronal ceroid lipofuscinosis

(Batten disease). Invest. Ophthalmol.Vis. Sci. *44*, 3725–3731.

Satoh, T., Nakamura, S., Taga, T., Matsuda, T., Hirano, T., Kishimoto, T., and Kaziro, Y. (1988). Induction of neuronal differentiation in PC12 cells by B-cell stimulatory factor 2/interleukin 6. Mol. Cell Biol. *8*, 3546–3549.

Schafer, K.H., Mestres, P., Marz, P., and Rose-John, S. (1999). The IL-6/sIL-6R fusion protein hyper-IL-6 promotes neurite outgrowth and neuron survival in cultured enteric neurons. J. Interferon Cytokine Res. *19*, 527–532.

Schindelin, J., Arganda-Carreras, I., Frise, E., Kaynig, V., Longair, M., Pietzsch, T., Preibisch, S., Rueden, C., Saalfeld, S., Schmid, B., et al. (2012). Fiji: an open-source platform for biological-image analysis. Nat. Methods *9*, 676–682.

Selvaraj, B.T., Frank, N., Bender, F.L., Asan, E., and Sendtner, M. (2012). Local axonal function of STAT3 rescues axon degeneration in the pmn model of motoneuron disease. J. Cell Biol. *199*, 437–451.

Shiomura, Y., and Hirokawa, N. (1987). Colocalization of microtubule-associated protein 1A and microtubule-associated protein 2 on neuronal microtubules in situ revealed with double-label immunoelectron microscopy. J. Cell Biol. *104*, 1575–1578.

Sims, S.M., Holmgren, L., Cathcart, H.M., and Sappington, R.M. (2012). Spatial regulation of interleukin-6 signaling in response to neurodegenerative stressors in the retina. Am. J. Neurodegener. Dis. *1*, 168–179.

Singh, R.D., Puri, V., Valiyaveettil, J.T., Marks, D.L., Bittman, R., and Pagano, R.E. (2003). Selective caveolin-1-dependent endocytosis of glycosphingolipids. Mol. Biol. Cell *14*, 3254–3265.

Sirajuddin, M., Rice, L.M., and Vale, R.D. (2014). Regulation of microtubule motors by tubulin isotypes and post-translational modifications. Nat.Cell Biol *16*, 335–344.

Söderberg, O., Gullberg, M., Jarvius, M., Ridderstråle, K., Leuchowius, K.J., Jarvius, J., Wester, K., Hydbring, P., Bahram, F., Larsson, L.G., and Landegren, U. (2006). Direct observation of individual endogenous protein complexes in situ by proximity ligation. Nat. Methods *3*, 995–1000.

Storer, M.A., Gallagher, D., Fatt, M.P., Simonetta, J.V., Kaplan, D.R., and Miller, F.D. (2018). Interleukin-6 regulates adult neural stem cell numbers during normal and abnormal post-natal development. Stem Cell Rep. *10*, 1464–1480.

Sulistio, Y.A., Lee, H.K., Jung, S.J., and Heese, K. (2018). Interleukin-6-mediated induced pluripotent stem cell (iPSC)-Derived neural differentiation. Mol. Neurobiol. *55*, 3513–3522.

Takemura, R., Okabe, S., Umeyama, T., Kanai, Y., Cowan, N.J., and Hirokawa, N. (1992). Increased microtubule stability and alpha tubulin acetylation in cells transfected with microtubule-associated proteins MAP1B, MAP2 or tau. J. Cell Sci. *103*, 953–964.

Thier, M., Marz, P., Otten, U., Weis, J., and Rose-John, S. (1999). Interleukin-6 (IL-6) and its soluble receptor support survival of sensory neurons. J. Neurosci.Res. *55*, 411–422.

Tran, A.D., Marmo, T.P., Salam, A.A., Che, S., Finkelstein, E., Kabarriti, R., Xenias, H.S., Mazitschek, R., Hubbert, C., Kawaguchi, Y., et al. (2007). HDAC6 deacetylation of tubulin modulates dynamics of cellular adhesions. J. Cell Sci. *120*, 1469–1479.

Verma, N.K., Dourlat, J., Davies, A.M., Long, A., Liu, W.Q., Garbay, C., Kelleher, D., and Volkov, Y. (2009). STAT3-stathmin interactions control microtubule dynamics in migrating T-cells. J. Biol. Chem. *284*, 12349–12362.

Wagner, J.A. (1996). Is IL-6 both a cytokine and a neurotrophic factor? J. Exp.Med. *183*, 2417–2419.

Wan, X.C., Trojanowski, J.Q., and Gonatas, J.O. (1982). Cholera toxin and wheat germ agglutinin conjugates as neuroanatomical probes: their uptake and clearance, transganglionic and retrograde transport and sensitivity. Brain Res. *243*, 215–224.

Wong, A.A., and Brown, R.E. (2012). A neurobehavioral analysis of the prevention of visual impairment in the DBA/2J mouse model of glaucoma. Invest. Ophthalmol.Vis. Sci. *53*, 5956–5966.

Yang, G., and Tang, Y.Y. (2017). Resistance of interleukin-6 to the extracellular inhibitory environment promotes axonal regeneration and functional recovery following spinal cord injury. Int. J. Mol.Med. *39*, 437–445.

Zahir-Jouzdani, F., Atyabi, F., and Mojtabavi, N. (2017). Interleukin-6 participation in pathology of ocular diseases. Pathophysiology *24*, 123–131.

Zhong, J., Dietzel, I.D., Wahle, P., Kopf, M., and Heumann, R. (1999). Sensory impairments and delayed regeneration of sensory axons in interleukin-6-deficient mice. J. Neurosci. *19*, 4305–4313.

STAR★METHODS

KEY RESOURCES TABLE

REAGENT or RESOURCE	SOURCE	IDENTIFIER
Antibodies		
polyclonal mouse anti-CD44 IgG	Abcam	RRID:AB_2847859
monoclonal mouse anti-Thy1.1/CD90 IgG	BD Pharmingen	RRID:AB_395586
goat anti-mouse IgG microbead-conjugated	Miltenyi Biotec	RRID:AB_244360
rat anti-mouse IgG1 microbead-conjugated	Miltenyi Biotec	RRID:AB_244354
anti-Brn3a (C-20) antibody	Santa Cruz	RRID:AB_2167511
anti-tubulin III antibody	BioLegend	RRID:AB_2566588
monoclonal Anti-beta-Tubulin III antibody	Sigma-Aldrich	RRID:AB_477590
monoclonal anti-tubulin, polyglutamylated (GT335)	Sigma-Aldrich	RRID:AB_477598
alpha-tubulin Antibody	Cell Signaling Technology	RRID:AB_2210548
Phalloidin-TRITC antibody	Sigma-Aldrich	RRID:AB_2315148
beta actin monoclonal antibody (AC-15)	ThermoFisher Scientific	RRID:AB_2536382
neurofilament, phosphorylated (SMI-31) Monoclonal	Covance	RRID:AB_10122491
anti-estrogen-related receptor beta antibody	Sigma-Aldrich	RRID:AB_262049
caveolin-1 (N-20) antibody	Santa Cruz	RRID:AB_2072042
anti-stathmin antibody, unconjugated	Cell Signaling Technology	RRID:AB_330234
rabbit anti-stathmin 1 antibody (SS0453)	Novus Biologicals	Cat#: NBP2-67169
MAP2 antibody [HM-2]	Abcam	RRID:AB_297885
Stat3 (79D7) rabbit mAb antibody	Cell Signaling Technology	RRID:AB_331269
STAT3 antibody [9D8]	Abcam	RRID:AB_10901752
mouse anti-STAT3 antibody (9D8)	Novus Biologicals	Cat#: NBP2-22471
rabbit anti-GAPDH monoclonal antibody, unconjugated, Clone 14C10	Cell Signaling Technology	RRID:AB_561053
GAPDH antibody [6C5]	Abcam	RRID:AB_2107448
Rat IL-6 Affinity Purified Polyclonal Ab antibody	R&D Systems	RRID:AB_355398
Alexa Fluor 488-AffiniPure Fab Fragment Donkey Anti-Mouse IgG (H+L) antibody	Jackson ImmunoResearch	RRID:AB_2340851
Alexa Fluor 488-AffiniPure Fab Fragment Donkey Anti-Rabbit IgG (H+L) antibody	Jackson ImmunoResearch	RRID:AB_2340620
Alexa Fluor 647 AffiniPure Fab Fragment Donkey Anti-Mouse IgG (H+L)	Jackson ImmunoResearch	Cat # 715-607-703
Alexa Fluor 647 AffiniPure Fab Fragment Donkey Anti-Rabbit IgG (H+L)	Jackson ImmunoResearch	Cat # 711-607-703
Rhodamine Red-X-AffiniPure Fab Fragment Donkey Anti-Mouse IgG (H+L) antibody	Jackson ImmunoResearch	RRID:AB_2340836
Rhodamine Red-X-AffiniPure Fab Fragment Donkey Anti-Rabbit IgG (H+L) antibody	Jackson ImmunoResearch	RRID:AB_2340615
IRDye 800CW Donkey anti-Rabbit IgG antibody	LiCor Biosciences	RRID:AB_2715510
IRDye 680RD Donkey anti-Mouse IgG antibody	LiCor Biosciences	RRID:AB_2814912
Biological samples		
Porcine Optic Nerve	Donated by Dr. James Jordan, Wake Forest School of Medicine	N/A

(*Continued on next page*)

Continued

REAGENT or RESOURCE	SOURCE	IDENTIFIER
Chemicals, peptides, and recombinant proteins		
cholera toxin subunit beta, Alexa Fluor conjugate	Life Technologies	Cat# C22841 and C22842
wheat germ agglutinin, Alexa Fluor conjugate	Life Technologies	Cat# W11261 and W11262
protein A superparamagnetic beads	Bio-Rad	Cat# 161-4013
Recombinant rat IL-6 protein	R&D Systems	Cat# 506-RL-050
Colchicine	Sigma-Aldrich	Cat# C9754
Critical commercial assays		
Duolink™*in situ* red starter kit	Sigma-Aldrich	Cat# DUO92101
SureBeads magnetic rack for IP	Bio-Rad	Cat# 1614813
Deposited data		
RNAseq data from WT versus *IL-6-/-* whole retina	This paper	GEO: GSE116916
Experimental models: Organisms/strain		
Mouse: *IL-6-/-*: B6.129S2-*IL6*^{tm1kopf}/J	The Jackson Laboratory	RRID:IMSR_JAX:002650
Mouse: WT: B6129SF2/J	The Jackson Laboratory	RRID:IMSR_JAX:101045
Rat: Sprague Dawley (for primary cell culture)	Charles River	Cat# Crl:SD
Software and algorithms		
SigmaPlot	Systat Software, Inc.	RRID:SCR_003210
SigmaStat	Systat Software, Inc.	RRID:SCR_010285
Fiji	N/A	RRID:SCR_002285
ImageJ	N/A	RRID:SCR_003070

RESOURCE AVAILABILITY

Lead contact

Further information and requests for resources and reagents should be directed to and will be fulfilled by the lead contact, Rebecca Sappington, Ph.D (rsapping@wakehealth.edu).

Materials availability

This study did not generate new unique reagents.

Data and code availability

- RNA sequencing data have been deposited at GEO and are publicly available as of the date of publication. Accession numbers are listed in the key resources table.
- This paper does not report original code.
- Any additional information required to reanalyze the data reported in this paper is available from the lead contact upon request.

EXPERIMENTAL MODELS AND SUBJECT DETAILS

Animals

All experiments complied with the ARVO statement for the use of animals in ophthalmic and vision research and were approved by the IACUC committees of Vanderbilt University Medical Center and Atrium Health Wake Forest Baptist.

Mice. Adult (2-3mo) male and female *IL-6–/–* mice (B6.129S2-*IL6*^{tm1kopf}/J; RRID:IMSR_JAX:002650; The Jackson Laboratory) and respective genomic controls (B6129SF2/J; RRID:IMSR_JAX:101045; The Jackson Laboratory) were used for all experiments. For experiments utilizing neonates, day of birth was designated P0. Mice were housed in accordance with NIH guidelines and maintained on a 12hr light/dark cycle with *ad*

libitum access to standard mouse chow and water. Littermates were randomly assigned to experimental groups.

Swine. Porcine optic nerve tissue was donated by Dr. James Jordan in the Department of Surgical Sciences – Cardiothoracic Surgery at Wake Forest School of Medicine.

Primary cell culture

Isolation of RGCs was carried out as previously described (Fischer et al., 2018, 2019). Eyes ($n \geq 16$/preparation) from postnatal day 2 to 4 Sprague-Dawley rats (Cat# Crl:SD; Charles River) were enucleated, retinas were dissected from each and stored on ice in Dulbecco modified Eagle medium plus 5% glucose (DMEM/glu; Gibco, Carlsbad, CA). Tissue was dissociated first by lightly vortexing for 10 seconds, and then by centrifugation (70xg for 6 min at 4°C). Retinas were triturated by pipetting and incubated for 15 min at 37°C in 1 mg/mL papain (Worthington, Lakewood, NJ) and 0.01% DNase I in Earle's Balanced Salt Solution. RGCs were purified by immunomagnetic separation, as previously described (Fischer et al., 2018, 2019). Briefly, to first remove Müller glia, the cell suspension was centrifuged (4°C at 250xg) and re-suspended in DMEM/Glu with a polyclonal mouse anti-CD44 IgG (4μg/mL, Cat#: ab157107; RRID:AB_2847859; Abcam). The suspension was incubated on ice for 10 min while shaking, before centrifugation (4°C at 250xg) and incubation on ice for 15 min, shaking, with anti-mouse IgG secondary antibody conjugated to magnetic microbeads (Cat# 130-048-401; RRID:AB_244360; Miltenyi Biotec, Auburn CA). The suspension was then loaded into a pre-equilibrated column in the presence of a magnetic field (Miltenyi Biotec). To isolate RGCs, the remaining cell suspension was incubated with monoclonal mouse anti-Thy1.1/CD90 IgG (5μg/mL; Cat#. 554895; RRID:AB_395586; BD Biosciences, San Diego CA) on ice, while shaking for 10 min, and then for 15 min on ice, shaking, with anti-mouse IgG1 secondary antibody conjugated to magnetic microbeads (IgG; Cat# 130-047-101; RRID:AB_244354; Miltenyi Biotec) and passed through a column in a magnetic field. The resulting Thy1.1/CD90-positive cells were plated into eight-chamber glass slides coated with laminin (0.01 mg/mL; Sigma) and grown in serum-free, B27-supplemented medium (Neuro-Basal; Gibco). The growth medium also contained 2 mM glutamine, 0.1% genomycin, 1% N_2 supplement (insulin 500 μg/mL; transferrin 10 mg/mL; progesterone 630 ng/mL; putrescine 1.6 mg/mL and selenite 520 ng/mL; Gibco), 50 ng/mL brain-derived neurotrophic factor (Invitrogen, Carlsbad, CA), 20 ng/mL ciliary neurotrophic factor (Invitrogen), 10 ng/mL bFGF (Invitrogen), and 100 μM inosine (Sigma). Before experiments, RGCs were maintained with the medium described above in a standard incubator containing 5% CO_2 until homeostasis was reached, as determined by neurite outgrowth and a stable level of viability (4 - 5 days).

METHOD DETAILS

Tissue preparation

For histological assays, mice were sacrificed by transcardial perfusion of 100ml of 1X PBS followed by 100ml of 4% PFA. Eyes, optic nerve and brain were processed as previously described (Echevarria et al., 2017; Fischer et al., 2019). For semi-thin and ultra-thin sectioning, optic nerves were post-fixed in 2.5% glutaraldehyde prior to epon embedding, as previously described (Sappington et al., 2003; Echevarria et al., 2017). For assays requiring fresh tissue, mice were sacrificed by cervical dislocation followed by decapitation. Eyes were enucleated and snap frozen on dry ice and stored at -80°C until use. Porcine optic nerve was obtained as fresh tissue at time of sacrifice by overdose and exsanguination. For histological studies, optic nerves were preserved by immersion fixation in 4% PFA at 4°C. For Western blot and Co-IP studies, optic nerves were flash frozen and stored at -80°C until use.

Anterograde axon transport measurements

Anterograde axonal transport capabilities of RGCs were assessed with CTB and WGA conjugated to a fluorophore, both established markers for active uptake and transport in the optic projection (Crish et al., 2010; Fernandez et al., 2012; Wong and Brown, 2012; Echevarria et al., 2017; Fischer et al., 2019). Briefly, mice were given a 1.5–2 μl intravitreal injection of CTB (10ug/μl in sterile PBS; Cat# C22841 and C22842; Life Technologies) or WGA (20ug/μl in sterile PBS; Cat# W11261 and W11262; Life Technologies) using a 33 gauge needle attached to a Hamilton syringe under 2.5% isoflurane anesthesia. 3 days after CTB/WGA injection, mice were sacrificed by transcardial perfusion as described above. Quantification of CTB/WGA signal in the SC and construction of retinotopic maps was done as previously described (Crish et al., 2010; Formichella et al., 2014; Echevarria et al., 2017; Duncan et al., 2018). Intact transport was defined

as percent area with CTB/WGA signal ≥70% density. Creation and quantification of 2D retinotopic map of ERRβ staining within the SC was done in a similar fashion. For experiments studying delayed CTB or WGA transport, mice were sacrificed 5 days after CTB/WGA injection. To confirm uniform CTB/WGA exposure to RGCs, a subset of whole-mount retinas were imaged *en montage* at 20X using confocal microscopy. For 3-day CTB tracing, n=12 (WT) and n=9 (*IL-6-/-*) superior colliculi. For 5-day CTB tracing, n=8 (*IL-6-/-*) superior colliculi. For 3-day WGA tracing, n=5 (WT) superior colliculi and n=10 (*IL-6-/-*) superior colliculi. For 5-day WGA tracing, n=7 (*IL-6-/-*) superior colliculi. Superior colliculi were excluded from analyses for poor injection, as confirmed by assessment of the retina and globe for successful tracer injection.

Immunohistochemistry

Labeling of whole-mount retinas, retinal cryosections, optic projections, floating brain sections and primary retinal ganglion cells were done as previously described (Echevarria et al., 2017; Duncan et al., 2018; Fischer et al., 2019). We used primary antibodies against Brn3a (1:50; Cat# sc-31984; RRID:AB_2167511; Santa Cruz) to visualize RGCs, β-Tubulin III (TUJ1, 1:500; Cat# 845501; RRID:AB_2566588; BioLegend), anti-α-tubulin (1:500; Cat# 2144S; RRID:AB_2210548; Cell Signaling Technologies), SMI-31 (1:1000; cat# SMI-31R-100; RRID:AB_10122491; Covance) and Phalloidin (actin, 1:50; Cat# P1951; RRID:AB_2315148; Sigma-Aldrich) to visualize RGCs and their axons or neurons in the brain, ERRβ (1:500; Cat# E0156; RRID:AB_262049; Sigma-Aldrich) to label RGC synaptic terminals in the SC, Cav-1 (1:250; Cat# sc-894; RRID:AB_2072042; Santa Cruz) to highlight Cav-1 localization in the retina and stathmin-1 (1:500; cat #3352; RRID:AB_330234; Cell Signaling Technologies), anti-MAP2 (1:500; Cat# ab11267; RRID:AB_297885; Abcam), and anti-GT335 (1:1000; Cat# T9822; RRID:AB_477598; Sigma-Aldrich) to highlight microtubule posttranslational changes and MAPs in axons. To visualize STAT3 in cells and tissue we used anti-mouse STAT3 (1:500; cat # ab119352; RRID:AB_10901752; Abcam). Secondary antibodies, if applicable, were used at a concentration of 1:200 and consisted of donkey anti-host species IgG conjugated to Alexa 488 (Cat # 715-547-003; RRID:AB_2340851or Cat # 711-547-003; RRID:AB_2340620; Jackson ImmunoResearch), Alexa 647 (Cat # 715-607-703; or Cat # 711-607-703; Jackson ImmunoResearch) or Rhodamine Red (Cat # 715-297-003; RRID:AB_2340836 or Cat # 711-297-003; RRID:AB_2340615; Jackson ImmunoResearch).

Epon embedding and electron microscopy

Epon embedding for semi-thin and ultra-thin sections was performed, as previously described (Sappington et al., 2003; Echevarria et al., 2017). Briefly, optic nerve segments were rinsed in cacodylate buffer and post-fixed in 1% osmium (OsO4) in cacodylate buffer for 30 minutes. Segments were then rinsed in cacodylate buffer, dehydrated in graded alcohol solutions, and embedded in Epon-Araldite. For semithin sections (700 nm), cross-sections of optic nerve near the chiasm were stained with 1% p-Phenylenediamine (PPD) and 1% toluidine blue to highlight myelin and glia, respectively (Echevarria et al., 2017). For electron microscopy, serial ultrathin sections were cut at 70 nm and photographed at 67000X resolution on a transmission electron microscope (Philips CM-12, 120 keV, Hillsboro, OR) in the Vanderbilt Cell Imaging Shared Resource.

RNA-Seq

Whole, intact retina was dissected from WT (n = 5) and *IL-6-/-* (n = 5) mice following sacrifice. Immediately following dissection, RNA was extracted from retina using TRIzol (Invitrogen, Cat# 15596026) and treated with deoxyribonuclease (DNase) I (Worthington, Cat# LS006333). Experiments were performed through the Vanderbilt Technologies for Advanced Genomics core at Vanderbilt University Medical Center. DNase-treated total RNA quality was assessed using the 2100 Bioanalyzer (Agilent Technologies). Samples with integrity values greater than 6 were used to generate polyA (mRNA)-enriched libraries, using stranded mRNA sample kits with indexed adaptors (New England BioLabs, Ipswich, MA). Library quality was assessed using the 2100 Bioanalyzer (Agilent Technologies) and libraries were quantitated using KAPA Library Quantification Kits (KAPA Biosystems, Wilmington, MA). Pooled libraries were subjected to 100bp paired-end sequencing according to the manufacturer's protocol (Illumina NovaSeq6000). Bcl2fastq2 Conversion Software (Illumina, San Diego, CA) was used to generate de-multiplexed Fastq files. Analysis of RNAseq results was performed through the Vanderbilt Technologies for Advanced Genomics Analysis and Research Design core at Vanderbilt University. Reads were aligned to the GENCODE GRCm38.p5 genome using STAR v2.5.3a. GENCODE vM12 gene annotations were provided to STAR to improve the accuracy of mapping. Quality control on raw reads was performed using FastQC. FeatureCounts v1.15.2 was used to count the number of mapped reads to each gene. Significantly differential expressed genes with adjusted p-value <0.05 and absolute fold change >2 were detected by DESeq2

v1.14. Data are reported as fold change (log scale) between WT and *IL-6-/-* retina. Data have been deposited in NCBI's Gene Expression Omnibus and are accessible through GEO series accession number GEO: GSE116916.

Proximity ligation assay

PLA assays in fixed tissue and fixed primary RGCs were carried out using the Duolink™*in situ* red starter kit (Cat #DUO92101, Sigma-Aldrich), using manufacturers protocols. Briefly, samples were first permeabilized with PBS + Triton X-100 0.4% for 10 min. The samples were then incubated with blocking solution for 30 min at 37°C and then with the primary antibodies for 1 hr at room temperature. Primary antibody concentrations used were: anti-STAT3 (1:500; cat #ab119352; RRID:AB_10901752; Abcam), anti-Stathmin-1 (1:500; cat #3352; RRID:AB_330234; Cell Signaling Technologies), anti-MAP2 (1:500; cat# ab11267; RRID:AB_297885; Abcam) and anti-β-tubulin (1:500; Cat# 801201; RRID:AB_2566588; BioLegend). Samples were washed twice for 5 min with buffer A, followed by incubation with the PLA probes in antibody diluent for 60 min at 37°C. After two washes of 5 min with buffer A, the ligation step was performed with ligase diluted in ligation stock for 30 min at 37°C. The samples were washed with buffer A twice for 2 min before incubation for 100 min with amplification stock solution at 37°C. Finally, samples were washed with 1x PBS and mounted with Duolink *in situ* mounting medium containing DAPI. For each experiment, a negative control experiment was performed where only one primary antibody was incubated with the PLA probes.

Immunoblotting

To extract whole protein from mouse retina, mouse optic nerve and pig optic nerve, we sonicated tissue in RIPA lysis buffer containing: 50mM Tris HCl, pH 7.2, 150nM NaCl, 1% NP-40, 1x Halt Protease and Phosphatase Inhibitor Cocktail (Cat# 78440; Thermo Scientific), and ddH20. Protein was collected as the supernatant following 10 min centrifugation (10,000rpm) at 4°C. The concentration of total protein was determined by BCA protein assay, as per manufacturer's instructions (Cat# 23225; Thermo Scientific). For mice, retina and optic nerves were pooled from 2 animals in each sample. Three samples were run per blot. For swine, protein was extracted from n = 12 optic nerves collected from n = 7 individual swine. Multiple samples were generated from each optic nerve for analysis across multiple Western blots. A total of n = 24 samples were run for Western blotting. Immunoblotting of whole protein lysates from retina and optic nerve was performed, as previously described (Duncan et al., 2017). For each Western blot, 20-30μg of protein in RIPA-Laemmli buffer with β-mercaptoethanol and loading buffer was loaded per lane. The following primary antibodies were used: anti-rabbit Cav-1 (1:250; Cat# sc-894; RRID:AB_2072042; Santa Cruz), anti-mouse β-actin (1:1000; Cat# AM4302; RRID:AB_2536382; ThermoFisher Scientific), mouse anti-β-tubulin (1:1000; Cat# T8660; RRID:AB_477590; Sigma-Aldrich), rabbit anti-α-tubulin (1:1000; Cat# 2144S; RRID:AB_2210548; Cell Signaling Technologies), anti-MAP2 (1:500; cat# ab11267; Cat# ab11267; RRID:AB_297885; Abcam), anti-GT335 (1:1000; Cat# T9822; RRID:AB_477598; Sigma-Aldrich), rabbit anti- or mouse anti- GAPDH (1:5000; Cat# 2118; RRID:AB_561053; Cell Signaling Technology; 1:5000; Cat# ab8245; RRID:AB_2107448; Abcam), mouse anti- or rabbit anti-STAT3 (1:1000; Cat# NBP2-22471, Novus Biologicals, Centennial, CO; 1:1000; Cat# 4904S; RRID:AB_331269; Cell Signaling Technology, Boston, MA), rabbit anti-stathmin (1:1000; cat# NBP2-67169; Novus Biologicals). Secondary antibodies utilized were donkey anti-mouse IRDye 680RD (1:1000; Cat# 925-68072; RRID:AB_2814912; Li-Cor) and donkey anti-rabbit IRDye 800CW (1:1000; Cat# 925-32213; RRID:AB_2715510; Li-Cor, Lincoln, NE). Molecular weight was determined by protein blotting standards (Cat# 1610376, Bio-rad, Hercules, CA). Bands were detected using the Odyssey Infared Imaging System (Li-Cor).

Co-Immunoprecipitation

Porcine optic nerve (n = 12 from 7 individual pigs) was cut into small pieces with a scalpel and placed in IP solution containing: Pierce IP Lysis Buffer (10μl/mg tissue; Thermo Scientific, #87787), 1x Halt Protease and Phosphatase Inhibitor Cocktail (cat# 78440, Thermo Scientific), and 1x EDTA Solution (Thermo Scientific #78440, 100x stock of each). Samples were homogenized by mortar and pestle (VWR 47747-366) followed by centrifugation (10,000 rpm) for 10 min at 40°C. The supernatant (whole protein) was removed and the concentration of protein determined by BCA protein assay, as per manufacturer's instructions (Cat# 23225; Thermo Scientific). Co-IP was conducted using the SureBeads magnetic system (Cat# 1614813; Bio-Rad). Prior to conjugation with stathmin antibody, protein A superparamagnetic beads (Bio-Rad # 161-4013) were magnetized and washed three times in 1ml PBS-T (1x PBS +0.1% Tween 20). For conjugation, rabbit anti-stathmin IgG (1:1000; Cat# NBP2-67169, Novus) was added to 100μl prepared protein A superparamagnetic beads and incubated for 20 minutes at room temperature. Conjugated beads and

antibody were collected by centrifugation, the beads were magnetized and the supernatant was discarded. Beads were re-magnetized and washed with PBS-T three times. Beads were then incubated with 300μg of the protein lysate from porcine optic nerve for 1 hour at room temperature. Sample and beads were collected by centrifugation, the beads were magnetized and the supernatant was discarded. Beads were re-magnetized and washed with PBS-T two times with a final wash in PBS only. All supernatants were discarded. Co-IP sample was eluted by a 10-minute incubation in 1x Laemmli buffer (cat# 1610747, Bio-rad) at 70°C followed by quick centrifugation. The resulting supernatant (Co-IP sample) was transferred to a new tube and processed for Western blotting against STAT3, as described above. The total number of Co-IP samples processed was n = 27.

Recombinant IL-6treatment. Primary RGC cultures (n≥4) were treated with either 10ng/ml or 1ng/ml recombinant rat IL-6 (1μg/μl; Cat # 506-RL-050, R&D Systems, Minneapolis, MN), as previously described (Sappington et al., 2006). Concentrations of 10ng/ml and 1ng/ml were selected based on previously published studies (Sappington et al., 2006; Fernando et al., 2014; Baran et al., 2018). Vehicle treatment consisted of an equivalent volume of culture media and carrier protein volume (0.1% BSA). To confirm that outcomes altered by recombinant IL-6 treatment were attributable directly to this treatment, we inhibited IL-6 activity with 10ng/ml IL-6 neutralizing antibody (ND50 = 0.03–0.09μg/mL; Cat# AF506; RRID:AB_355398; R&D Systems), as previously described (Sappington et al., 2006). Following 4 days of treatment with RGC cultures, cells were fixed with 4% PFA and processed for either immunocytochemistry or proximity ligation assay.

Colchicine treatment. Primary RGC cultures (n≥4) were pre-treated for 1 hour with either vehicle, recombinant rat IL-6 (1ng/ml) or recombinant rat IL-6 (1ng/ml) plus neutralizing antibody (10ng/ml), as outlined above. Following IL-6 and antibody pre-treatments, RGC cultures were exposed to 1mM colchicine (Cat# C9754;Sigma-Aldrich) for 1 hour. The concentration of colchicine was determined by previous studies examining microtubule destabilization and long-term activities of colchicine (Gibbs et al., 1980; Emons et al., 1990). After 2 hours of total treatment time, cultures were fixed and immunolabeled with antibodies against β-tubulin, as described above.

QUANTIFICATION AND STATISTICAL ANALYSIS

Quantification of RGC soma and axons

For RGC density, 5-7 pseudo-random z-stack images were taken throughout the mid –peripheral/mid-central retina (n=3/genotype) at 60X using an Olympus confocal microscope, as previously described (Duncan et al., 2018). TUJ1/SMI31 dual positive RGCs were counted from each image and divided by the area of the counting field (0.101mm^2) to get RGC density. Semi-thin sections of optic nerve were imaged *en montage* at 100x magnification on an upright Olympus (Melville, NY) microscope. Total axon diameter (myelin sheath + axon) and inner axon diameter (axon only) was measured, using NIS-Elements AR. Myelin thickness was calculated as total axon diameter minus inner axon diameter divided by 2. The gRatio was calculated as the inner axon diameter divided by the total axon diameter. In each nerve, 35 axons were measured. For WT mice, 8 nerves from 7 animals were analyzed (280 total measurements). For *IL-6-/-* mice, 9 nerves from 9 animals were analyzed (315 total measurements).

Protein concentration

For semi-quantitative measurement of protein expression, protein bands in western blots were subjected to densitometry analysis (Odyssey Application Software V3.0; Li-Cor) and normalized to densitometry of β-actin or GAPDH. All samples used for densitometry analysis were run on the same gel and transferred to the same nitrocellulose membrane.

PLAsignal intensity

In primary RGC cultures (n = 4 - 6), PLA signal in neurites was quantified as integrated density of fluorescence, using ImageJ (RRID:SCR_003070). To measure changes in PLA signal in neurites specifically, soma were manually traced and masked for measurement and calculation of integrated density.

Scholl analysis

Sholl analysis was carried out on RGC cultures receiving colchicine experimentation, using Scholl analysis software in Fiji (RRID:SCR_002285), as previously described (Schindelin et al., 2012; Ferreira et al., 2014; Bird and Cuntz, 2019). Briefly, from each 40X confocal image, a single RGC was identified. The RGC soma and

processes were traced in Fiji (RRID:SCR_002285) using the pencil tool. The image format was adjusted to 8-bit to create a black and white image, and then the threshold of the image was altered to create a binary image, showing the cell soma and processes only. The center of the cell soma was identified using a point marker and Scholl analysis carried out in Fiji (RRID:SCR_002285), using 5μm concentric rings radiating from the cell soma. The number of intersections of neurites was determined at each concentric ring by the Scholl analysis software. Data from $n \geq 5$ RGCs per condition was plotted in SigmaPlot (versions 11.1 and 13.0; RRID:SCR_003210).

Statistics

Statistical analysis were done using SigmaPlot with SigmaStat (versions 11.1 and 13.0; RRID:SCR_003210 and RRID:SCR_010285). For two independent variables that passed normality and equal variance tests, we determined statistical significance with a two-sided t-test. For two variables arising from the same sample (i.e. Western blotting), we assess normality by the Shapiro-Wilk method and determined statistical significance with a paired t-test. For datasets that did not meet normality (Shapiro-Wilk) and/or equal variance (Brown-Forsythe) requirements, we utilized a Mann-Whitney Rank Sum Test. For multiple variable comparisons, we performed a one-way analysis of variance with pairwise comparison by the Holm-Sidak method. For multiple variable comparisons that did not meet normality (Shapiro-Wilk) and/or equal variance (Brown-Forsythe) requirements, we performed a Kruskal-Wallis one-way analysis of variance on ranks followed by pairwise comparisons with Dunn's Method. *Post hoc p* values less than 0.05 were considered statistically significant. Number of measurements and specific *p*-values are indicated in results or figure legends.